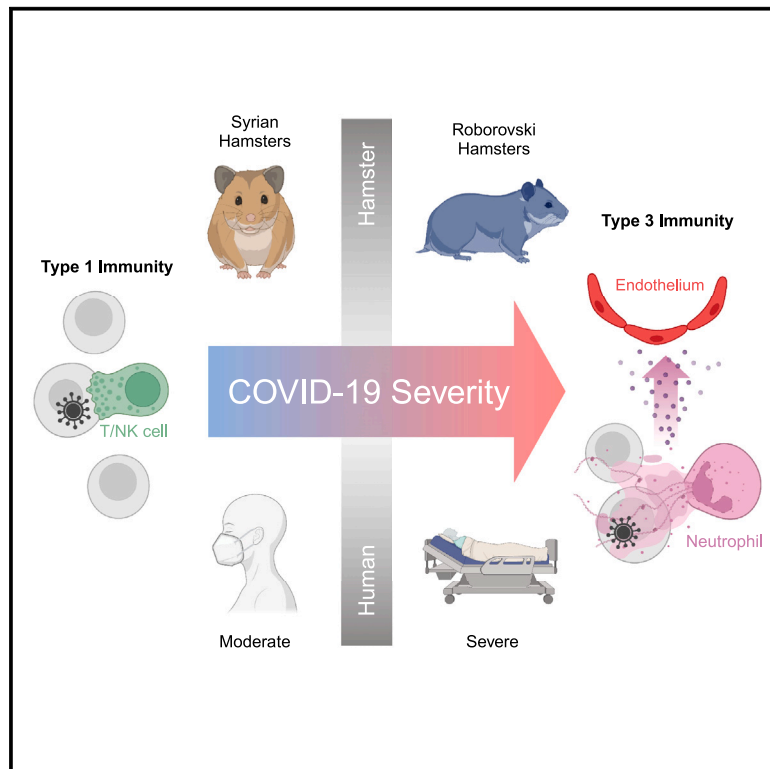# Single-cell-resolved interspecies comparison shows a shared inflammatory axis and a dominant neutrophil-endothelial program in severe COVID-19

Graphical abstract

Authors

Stefan Peidli, Geraldine Nouailles, Emanuel Wyler, ..., Jakob Trimpert, Markus Landthaler, Samantha D. Praktiknjo

Correspondence

samantha.praktiknjo@bih-charite.de

In brief

Peidli et al. combine specialized machine learning with time-resolved single-cell RNA datasets of humans and established hamster models to elucidate cell-type-specific responses that lead to either reversible or terminal inflammation and damage of lung tissues upon SARS-CoV-2 infection.

Highlights

- Humans and hamsters share a common inflammatory response to SARS-CoV-2

- Disease severity correlates with early innate effector cell-type response

- Diffusion-based analyses dissect neutrophil and endothelial cell responses during infection

- Differences in cell-type responses lead to either reversible or terminal endothelial damage

Article

Single-cell-resolved interspecies comparison shows a shared inflammatory axis and a dominant neutrophil-endothelial program in severe COVID-19

Stefan Peidli,[1,2,11,14] Geraldine Nouailles,[3,14] Emanuel Wyler,[4] Julia M. Adler,[5] Sandra Kunder,[6] Anne Voß,[6] Julia Kazmierski,[7,8,12] Fabian Pott,[7,8] Peter Pennitz,[3] Dylan Postmus,[7,8,13] Luiz Gustavo Teixeira Alves,[4] Christine Goffinet,[7,8,13] Achim D. Gruber,[6] Nils Blüthgen,[1,2] Martin Witzenrath,[3,9] Jakob Trimpert,[5,10,15] Markus Landthaler,[2,4,15] and Samantha D. Praktiknjo[8,15,16,*]

[1]Charité - Universitätsmedizin Berlin, Corporate Member of Freie Universität Berlin and Humboldt-Universität zu Berlin, Institute of Pathology, Berlin, Germany
[2]Institute for Biology, Humboldt-Universität zu Berlin, Berlin, Germany
[3]Charité - Universitätsmedizin Berlin, Corporate Member of Freie Universität Berlin and Humboldt-Universität zu Berlin, Department of Infectious Diseases, Respiratory Medicine and Critical Care, Berlin, Germany
[4]Berlin Institute for Medical Systems Biology (BIMSB), Max Delbrück Center for Molecular Medicine in the Helmholtz Association (MDC), Berlin, Germany
[5]Institut für Virologie, Freie Universität Berlin, Berlin, Germany
[6]Institute of Veterinary Pathology, Freie Universität Berlin, Berlin, Germany
[7]Charité - Universitätsmedizin Berlin, Corporate Member of Freie Universität Berlin and Humboldt-Universität zu Berlin, Institute of Virology, Berlin, Germany
[8]Berlin Institute of Health at Charité – Universitätsmedizin Berlin, Berlin, Germany
[9]German Center for Lung Research (DZL), Berlin, Germany
[10]Department of Diagnostic Medicine and Pathobiology, College of Veterinary Medicine, Kansas State University, Manhattan, KS, USA
[11]Present address: European Molecular Biology Laboratory, Heidelberg, Germany
[12]Present address: Gladstone Institute of Virology, San Francisco, CA, USA
[13]Present address: Department of Tropical Disease Biology, Liverpool School of Tropical Medicine, Liverpool, UK
[14]These authors contributed equally
[15]Senior author
[16]Lead contact
*Correspondence: samantha.praktiknjo@bih-charite.de
https://doi.org/10.1016/j.celrep.2024.114328

SUMMARY

A key issue for research on COVID-19 pathogenesis is the lack of biopsies from patients and of samples at the onset of infection. To overcome these hurdles, hamsters were shown to be useful models for studying this disease. Here, we further leverage the model to molecularly survey the disease progression from time-resolved single-cell RNA sequencing data collected from healthy and severe acute respiratory syndrome coronavirus 2 (SARS-CoV-2)-infected Syrian and Roborovski hamster lungs. We compare our data to human COVID-19 studies, including bronchoalveolar lavage, nasal swab, and postmortem lung tissue, and identify a shared axis of inflammation dominated by macrophages, neutrophils, and endothelial cells, which we show to be transient in Syrian and terminal in Roborovski hamsters. Our data suggest that, following SARS-CoV-2 infection, commitment to a type 1- or type 3-biased immunity determines moderate versus severe COVID-19 outcomes, respectively.

INTRODUCTION

For coronavirus disease 2019 (COVID-19), caused by infection with severe acute respiratory syndrome coronavirus 2 (SARS-CoV-2), a range of cellular and molecular processes have been associated with the first acute disease phase.[1,2] Among them, innate immunity responses particularly have been shown to be essential in modulating severe/critical COVID-19, ultimately leading to an overly exacerbated inflammatory state and the production of proinflammatory cytokines.[3–9] This has been exten-

sively described for pulmonary macrophages[10,11] but also for neutrophils, which contribute to disease severity through thrombotic complications caused by NETosis.[12,13]

Animal models have been essential in the study of COVID-19[14,15]. Hamsters have been particularly useful as they can be readily infected by the same SARS-CoV-2 variants as humans.[16,17] A key advantage of animal models is that samples can be taken from the earliest time point after infection—unlike patient samples, which are typically collected at least 1 week post infection due to incubation times and study enrollment.
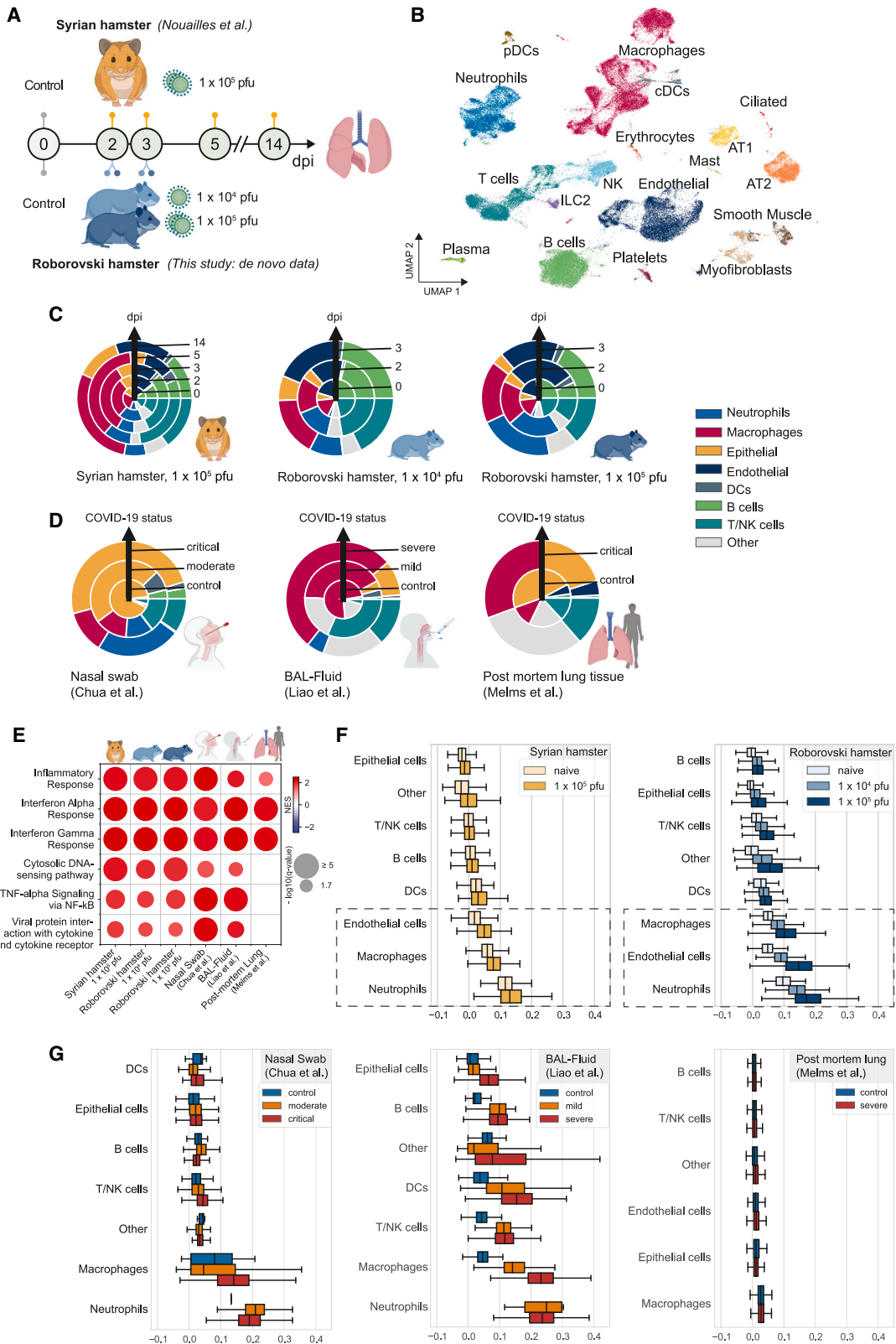
(legend on next page)

Furthermore, animal models allow for investigation of samples, such as whole lung tissue, that cannot be obtained from humans due to medical and ethical constraints, thus allowing researchers to identify early processes of innate immunity that are fundamental in determining a mild or severe COVID-19 course and to longitudinally study disease progression.

Here, we provide a comprehensive single-cell RNA sequencing (scRNA-seq) study of the dynamic cellular and molecular pulmonary landscape underlying different COVID-19 outcomes. Specifically, based on the observations that Syrian hamsters (*Mesocricetus auratus*) experience a moderate course of disease, whereas Roborovski hamsters (*Phodopus roborovskii*) suffer from severe to lethal COVID-19,[16,18] we established a time-resolved resource of scRNA-seq data collected from healthy and SARS-CoV-2-infected lung tissue of both hamster species, which we extensively compared to published human data. Using a range of analysis methods, including *post hoc* interpretation methods in cell-type-specific diffusion map latent spaces, we found neutrophils and endothelial cells to be likely instrumental in regulating severe courses of COVID-19, and we identified expression programs that associate with progressive endothelial damage.

RESULTS

Tracking cellular changes throughout SARS-CoV-2 infection

To identify the cells and early molecular markers that regulate COVID-19 disease severity, we jointly analyzed pulmonary scRNA-seq time-course data from two different hamster species modeling moderate and severe COVID-19. Specifically, we reprocessed our previously published data for Syrian hamsters[19] and generated *de novo* Roborovski hamster scRNA-seq datasets for this study, which we further compared to publicly available human data[20–22] (Figure 1).

Syrian hamsters develop moderate COVID-19 and recover from infection[28]; therefore, analysis time points range from uninfected "naive" control animals (0 days post infection [dpi]) to early onset (2 dpi) over acute phase of infection (3 and 5 dpi) to recovery at 14 dpi. Roborovski hamsters develop an overall more severe course of disease, with fulminant pneumonia when infected with 1×10^5 plaque-forming units (pfu) and with less striking but still considerable COVID-19-like disease when infected with 1×10^4 pfu of SARS-CoV-2. Time-course data comprise naive (0 dpi) and acute phase (2 and 3 dpi), as severe course hamsters do not recover from disease and reach humane endpoint criteria from 3 dpi onward (Figure 1A). Objective clinical signs of SARS-CoV-2 infection are dominated by weight loss in Syrian hamsters[19] but include more severe signs of disease such as drop of body temperature as well as reduced movement and fur care up to the point of lethargy in Roborovski hamsters that experience a severe course of infection (Figure S1A, Trimpert et al.[18]). scRNA-seq hamster datasets displayed high quality and little variation across replicates (Figures S1B and S1C), enabling us to identify all major cell types of the lungs (Figure 1B), including the primary target of SARS-CoV-2: alveolar type 2 (AT2) cells.[29] In addition, we established a customized data preprocessing pipeline (see STAR Methods) that allows the recovery of many neutrophils that are typically discarded during filtering steps. Virus sequences were enriched in professional phagocytes (macrophages, neutrophils) (Figure S1D).

In order to relate the cellular composition of infected hamster lungs to human COVID-19 patients, we collected public scRNA-seq data from human nasal swab,[20] bronchoalveolar lavage (BAL) fluid,[21] and postmortem lung tissue[22] samples. Direct comparison was hampered by different sample types, time of sampling, and variable quality of human single-cell datasets generally containing a lower complexity of cell types. Nevertheless, we observed shared COVID-19-specific trends. This particularly includes neutrophils, for which the proportion increased after infection across species and sample types, with the exception of postmortem lung tissue, for which no neutrophils could be detected (Figures 1C and 1D). The increase in neutrophils was most pronounced in critical/severe human patients and Roborovski hamsters irrespective of virus dose, compared to a weaker rise in patients with mild/moderate COVID-19 and Syrian hamsters. Furthermore, T and natural killer (NK) cell proportions increased in human nasal swab and BAL-fluid samples after infection and Syrian hamsters toward

Figure 1. The single-cell landscape of SARS-CoV-2-infected lungs

(A) Study design outlining hamster data used in this study. Syrian and Roborovski hamsters were collected naively (uninfected, control animals) or challenged with SARS-CoV-2 (1×10^4 pfu or 1×10^5 pfu SARS-CoV-2 variant B.1, as indicated). Syrian hamster dataset was taken from Nouailles et al.,[19] comprising scRNA-seq data from lung tissue collected at 0 (naive, uninfected controls), 2, 3, 5, and 14 days post infection (dpi) with 1×10^5 pfu SARS-CoV-2 ($n = 3$ control animals + $n = 3$ replicates $\times$ 4 time points = 15). Additionally, Roborovski hamsters were treated with either 1×10^4 pfu or 1×10^5 pfu SARS-CoV-2, and scRNA-seq data generated from lung tissue collected at 0 (naive, uninfected controls), 2, and 3 dpi ($n = 3$ control animals + 3 replicates $\times$ 2 dosages $\times$ 2 time points = 15); 30 animals total.

(B) Integrated uniform manifold approximation and projection (UMAP) embedding of Syrian and Roborovski scRNA-seq samples with individual cells colored by cell type.

(C) Cell proportions per hamster species and virus dose colored by cell type. Each ring corresponds to a time point after infection in ascending order from the center outward.

(D) As in (C), but for human datasets and with rings corresponding to COVID-19 status.

(E) Selected significant gene sets ($p < 0.05$) from gene set enrichment analysis (GSEA)[23] performed on genes differentially expressed in infected (2 and 3 dpi) vs. control samples across datasets. Color corresponds to normalized enrichment score (NES) and dot size to −log10(q value). Gene sets from Kyoto Encyclopedia of Genes and Genomes (KEGG)[24–26] and MSigDB Hallmarks.[27]

(F) Inflammatory response scores (Hallmark gene set, MSigDB; see STAR Methods) across cell types in Syrian and Roborovski hamsters in infected (2 and 3 dpi) and naive samples.

(G) As in (F), but for human datasets split by COVID-19 status.

(F and G) Boxplots: box represents quartiles; line represents median; whiskers represent quartiles plus 1.5 times interquartile range; outliers not shown.
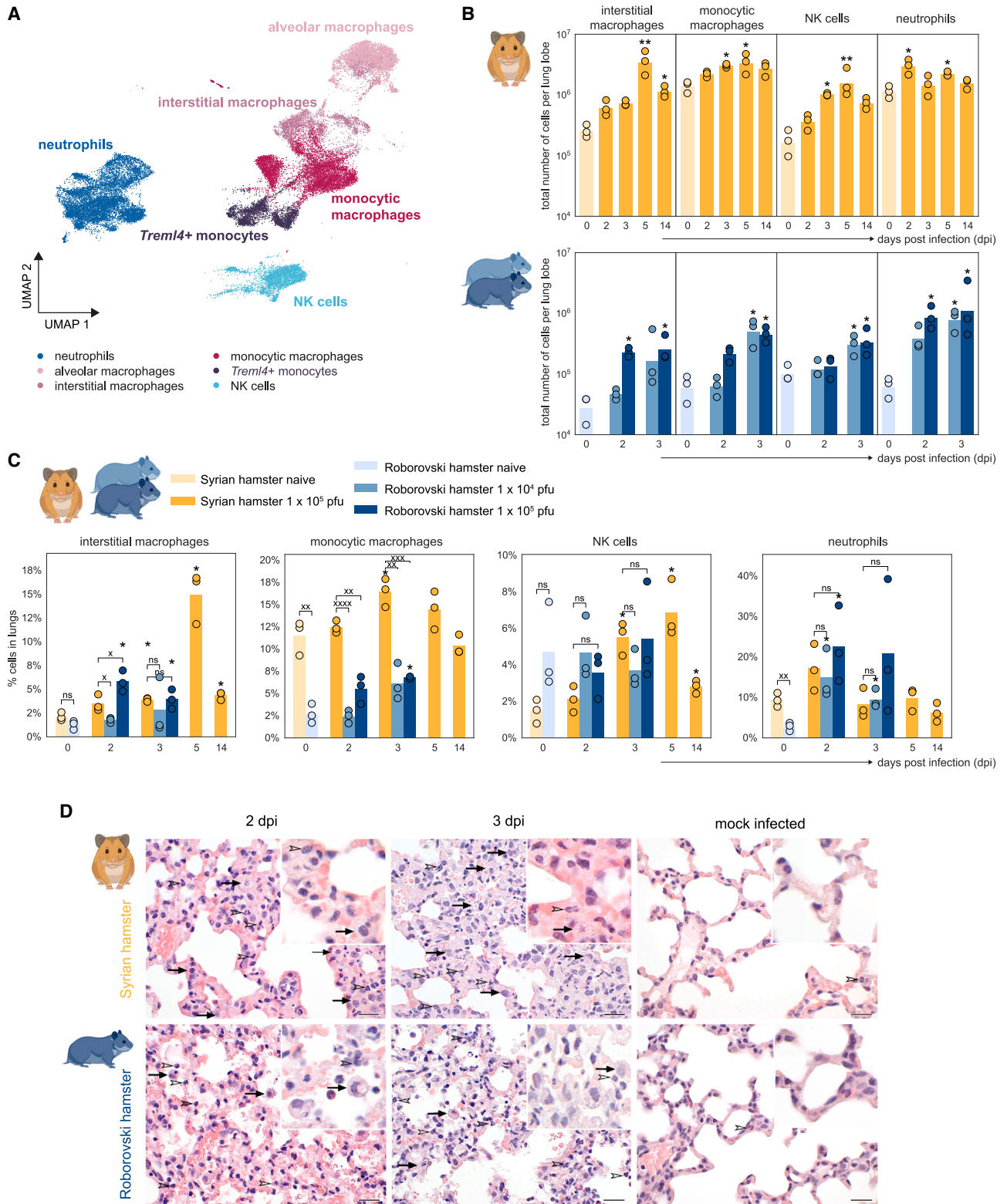
(legend on next page)

5 dpi. This was not observed in Roborovski hamsters, which might be due to the lack of corresponding samples from later stages of infection.

Beyond changes in cell frequency, we sought to identify cell types most strongly reacting to the infection. We therefore performed a global pathway enrichment analysis and found inflammatory genes to be highly enriched following SARS-CoV-2 infection throughout all hamster and human datasets (Figures 1E and S1E; see STAR Methods). In both hamster species, neutrophils showed the strongest inflammatory activity among all cell types at the early onset and acute phase of infection (Figure 1F), followed by macrophages. This finding also applied to human BAL fluid and nasal swab (Figure 1G). Moreover, we found that endothelial cells were strongly affected by the infection in lung tissues, with Roborovski hamsters having a markedly higher inflammation score than their Syrian hamster counterparts. Unlike BAL fluid and nasal swab, human postmortem lung tissue contained endothelial cells. However, data quality was overall low in this sample type with absence or extremely weak presence of detectable molecular signals. As a result, the feasibility of conducting further molecular investigation using this sample type was limited (Figure 1G).

SARS-CoV-2 infection causes cellular disbalance of innate immune cells

Innate immune cells in patients and animal models reacted strongly to SARS-CoV-2 infection, both in terms of composition and inflammatory gene expression profiles. We thus investigated these cells at higher resolution in lungs (Figure 2A). By reintegrating and subclustering the respective cell populations, we were able to identify neutrophils and NK cells using canonical marker expression, in addition to four different subtypes of monocytes/macrophages including interstitial macrophages (IMs), monocytic macrophages (MoMs), alveolar macrophages (AMs), and $Treml4^+$ monocytes.[19]

We forewent direct comparison of cell numbers per lobe between Syrian and Roborovski hamsters due to different animal and, consequently, lung sizes (Figure 2B). Overall, pulmonary numbers of IMs, MoMs, NK cells, and neutrophils increased significantly ($p < 0.05$) in both species during infection. In Syrian hamsters, IMs, MoMs, and NK cell numbers peaked at 5 dpi, whereas the highest neutrophil numbers were detected at 2 dpi (Figure 2B). Due to the short observation window, resolution of innate cellular responses was not observed in Roborovski hamsters (Figure 2B). To further identify dominating immune cell types and for direct comparison between related species, we tracked cellular proportions, which reflect local proliferation and cellular influx (Figure 2C). IM proportions increased fastest (2 dpi, ~6%) upon high-dose infection of Roborovski hamsters, but they remained at similar levels by 3 dpi. In Syrian hamsters, IMs peaked by far highest, with ~15% among lung cells at 5 dpi, yet resolved close to baseline levels by 14 dpi. MoM proportions were high (~11%) in naive (0 dpi) Syrian hamsters, yet they significantly increased ($p = 0.035$) to ~16% by 3 dpi. Similarly, MoMs increased significantly ($p = 0.045$) upon high-dose infection in Roborovski hamsters from ~2% to ~7% by 3 dpi. In contrast, the proportion pattern for NK cells and neutrophils differed between species. While NK cells significantly increased by 2-fold at 3 dpi compared to 0 dpi ($p = 0.0027$) and peaked with ~7% at 5 dpi ($p = 0.008$) in Syrian hamsters, SARS-CoV-2 infection did not trigger an increase in NK cell frequencies in Roborovski hamsters. Frequencies of neutrophils, however, increased significantly in Roborovski hamsters from ~2% in naive animals to ~15% and ~20% at 2 dpi upon low- and high-dose infection ($p = 0.023$), respectively. Notably, only upon high-dose infection did Roborovski hamsters maintain high neutrophil frequencies at 3 dpi. Syrian hamsters had higher baseline proportion of neutrophils (~10%). However, neutrophils only modestly increased to ~17% at 2 dpi, and had already started resolving at 3 dpi to baseline levels (Figure 2C). In contrast, AMs and $Treml4^+$ monocytes did not respond as strongly to infection (Figures S2A and S2B).

Histopathological examination revealed slightly higher numbers of cells consistent with macrophages in Syrian compared to Roborovski hamsters at 2 and 3 dpi despite similarly high infectious dose (Figure 2D). Alveolar wall necrosis in Roborovski hamsters was generally more apparent when compared to Syrian hamsters at both time points, particularly at 3 dpi. Notably, Syrian hamsters developed the first signs of epithelial cell proliferation and tissue regeneration at 3 dpi, resulting in a markedly higher density of parenchymal cells and thicker alveolar walls when compared to the more damaged and necrotic alveolar walls in Roborovski hamsters (Figure 2D).

Different cell-mediated immune programs are activated upon infection

The observed differences in innate immune cell composition upon infection indicate that different immunological programs are activated in Syrian and Roborovski hamsters. Innate and adaptive cell-mediated effector immunity can be discriminated into three types.[30] Type 1 immunity is directed toward intracellular pathogens and achieves this primarily through the

---

Figure 2. Disproportionate innate immune cell response throughout SARS-CoV-2 infection

(A) UMAP embedding of innate immune cells. Subclustering identified four distinct types of macrophages.

(B) Total number of cells per selected cell type in lung lobe across dpi, split by Syrian and Roborovski hamsters and additionally by virus dose for the latter, indicated by color. Test for difference in distribution across samples ($n = 3$; one-way ANOVA with Dunn *post hoc* test) against corresponding uninfected samples. *$p < 0.05$, **$p < 0.01$.

(C) Relative numbers of cell types as shown in (B). Additional test for difference in distribution, as described in (B), and across hamster types within time points. x < 0.05, xx < 0.01, xxx < 0.001, xxxx < 0.0001.

(D) Representative histopathological findings in Syrian and Roborovski hamsters at 2 and 3 dpi. Comparison showing more cells compatible with macrophages (black arrows) in Syrian hamsters (top) than Roborovski hamsters (bottom). The numbers of infiltrating neutrophils (open arrowheads) appeared to be similar in both species (see also Figure S7 for histopathological examination of neutrophils). Hamster lungs at 2 (left) and 3 (middle) dpi or mock infected with PBS (right), H&E stain, original magnification = 600-fold or 1,000-fold (inserts); scale bars, 20 μm. Infection with 1×10^5 pfu SARS-CoV-2.
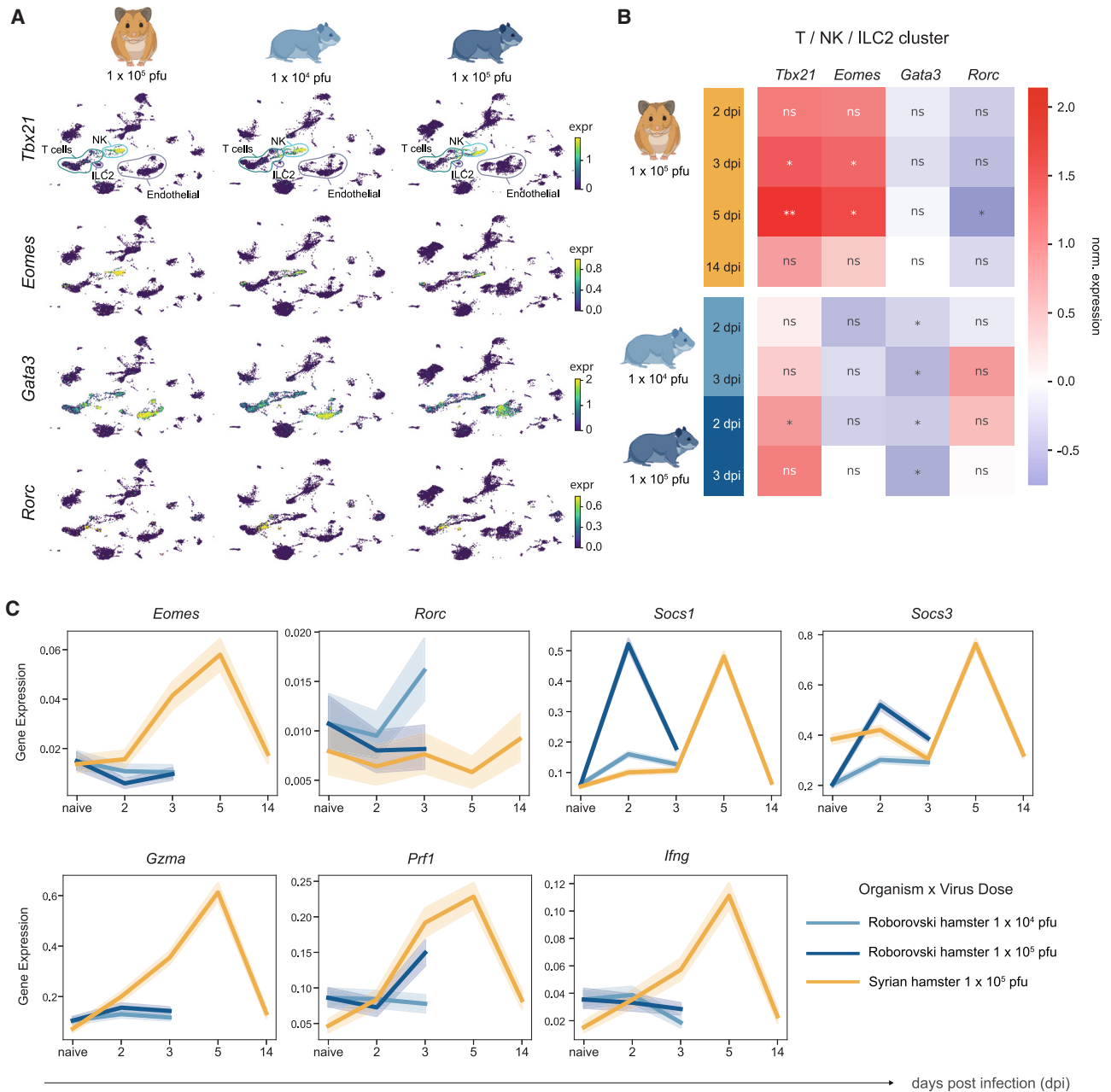
Figure 3. Roborovski and Syrian hamsters commit to different types of immunity

(A) Normalized gene expressions of selected immunity-related TFs at 2 and 3 dpi for shown hamster species and virus dose. Integrated UMAP embeddings as in Figure 1B with relevant cell types showcased in the first row.

(B) Sample-wise $\log_2$ fold changes of normalized gene expression with respect to corresponding uninfected samples for genes in (A) after pseudobulking T cell, NK cell, and ILC2 clusters. The p values of t tests for difference in significance across samples ($n = 3$) are marked with *$p < 0.05$, **$p < 0.01$, or ns (not significant).

(C) Averaged normalized expression of immunity-related genes for all cells across time colored by hamster species and virus dose. Transparent areas show 95% confidence intervals computed by bootstrap sampling.

activation of macrophages and cytotoxic effector cells. Type 2 immunity targets helminths and stimulates mucus production and activation of mast cells, eosinophils, and basophils. Type 3 immunity is directed toward extracellular pathogens such as bacteria or fungi. Its effector modules trigger epithelial barrier defense and neutrophil recruitment.

In contrast to accessory cells, such as neutrophils and macrophages, which lack intrinsic specificity and are recruited to participate in a given immune response, NK cells, innate lymphoid cells (ILCs), and T cells express type-defining transcription factors (TFs). We therefore examined these cell types in the single-cell data in order to identify the dominant type of immunity

(Figures 3A and 3B). In accordance with preferential NK cell recruitment, we observed an increase of type 1 immunity-associated TF expression (*Eomes*, *Tbx21*)[31] in lungs of Syrian hamsters, which was largely absent or weaker in Roborovski hamsters (Figure 3B). The expression of these markers was confined to NK cells and partially to CD4⁺ T cells (Figure 3A). Next, to gain deeper insights into a potential type 1 versus type 3 immunity bias, we visualized selected effector molecules, key cytokine and immune regulatory genes across time and all cell types, to further evaluate the induced immune type (Figures 3C and S3A). The expression of *Eomes* clearly increased in Syrian until 5 dpi, while this trend was entirely absent in Roborovski hamsters. Additionally, the expression of typical cytotoxic effector molecules such as *Gzma*, *Prf1*, and key type 1 cytokine *Ifng* followed similar trends in Syrian hamsters, while there was no consistent upregulation of *Gzma* and *Ifng* in lungs of Roborovski hamsters (Figure 3C). Despite the predominant neutrophil response in Roborovski hamsters, the primary TF associated with type 3 immunity (*Rorc*) displayed no clear upregulation over time and all cells in high-dose-infected Roborovski hamsters (Figure 3C). However, focusing on the NK, T, and ILC clusters, *Rorc* expression significantly decreased at 5 dpi in Syrian hamsters (*p* = 0.02) and showed a trend toward upregulation at 2 dpi in high-dose- and at 3 dpi in low-dose-infected Roborovski hamsters (Figure 3B). The type 2 immunity TF *Gata3* was expressed in ILC2 and endothelial cell subsets as expected[32,33] (Figure 3A), while no upregulation upon infection was observed in the T/NK/ILC subset (Figure 3B). Suppressor of cytokine signaling (SOCS) proteins regulate innate and adaptive immunity and can thereby shape initiation and maintenance of immune type. Broadly, SOCS1 suppresses type 1 and SOCS3 type 3 immunity.[34] We found that, at 2 dpi, *Socs1*, *Stat1*, and *Il6* were strongly upregulated in Roborovski hamsters upon high-dose infection (Figures 3C and S3A). In Syrian hamsters, *Socs1* and *Socs3* were both upregulated at the peak cellular response at 5 dpi (Figure 3C), and expression of *Il12a*, *Stat4*, and *Stat3* was generally higher compared to Roborovski hamsters (Figure S3A). Similarly, upon infection, *Ifng*, *Gzma*, and *Prf1* displayed uniform upregulation in Syrian hamsters in the T/NK/ILC subset, while *Stat1* and *Socs1* showed highest upregulation in high-dose-infected Roborovski hamsters. *Stat4* and *Stat3*, however, displayed no clear trend toward upregulation or a specific hamster species bias in the T/NK/ILC subset (Figure S3B). In summary, the underlying gene expression profiles in Syrian and Roborovski hamsters broadly match the observed cellular effector responses, reinforcing a type 1 in Syrian versus type 3 bias in Roborovski hamsters.

Neutrophils share a common inflammatory state with variable intensity

The strength of the neutrophil response differed drastically between our COVID-19 hamster models and might determine their lethality. To better understand differences in quality of the neutrophil response to SARS-CoV-2, we used a factor analysis approach using diffusion maps[35,36] to create a low-dimensional embedding of all neutrophils in Syrian and Roborovski hamsters (Figure 4A). Briefly, diffusion map is a dimensionality reduction method similar to principal-component analysis (PCA), but unlike PCA, it defines dominant axes of variation across cells based on

random walk distances. The components extracted by diffusion map describe continuous relationships between cells and thereby more adequately model the biology within cell types than classical cluster-based analysis (see STAR Methods).

In this latent space, we identified the first diffusion component (DC1) as the leading variable associated with inflammatory neutrophil responses. This inflammatory axis was characterized by the expression of several inflammatory pathways, including JAK-STAT, RIG-I, and tumor necrosis factor (TNF) α signaling (Figure 4B). Therefore, we further analyzed this component and visualized the distribution of neutrophils along DC1 for each time point (Figure 4C). At 0 dpi, neutrophils were localized on the left side of DC1. However, upon infection, there was a general shift to the right side of DC1 for the entire neutrophil population. Specifically, upon high-dose infection, Roborovski hamster neutrophils massively overshot Syrian and low-dose-infected Roborovski hamster neutrophils to the far right at 2 dpi. In contrast, Syrian hamster neutrophils progressively moved along DC1, reaching the furthest positions at 5 dpi, before completely returning to the original 0 dpi DC1 "ground state" at 14 dpi.

To identify the molecular drivers that describe DC1, we next ranked genes according to their correlation with the DC1 axis (Figures 4D and S4A). The left side of DC1 associated with high expression of genes that gradually decreased toward high DC1. These included *S100a8* and *S100a9*, known to compose half of the neutrophils' cytoplasmic proteins and to act as damage-associated molecular patterns (DAMPs) in inflammation. They critically modulate leukocyte recruitment, cytokine secretion, and neutrophil activation.[37,38] Accordingly, the right side of DC1 was marked by increased expression of interferon-stimulated and chemokine-encoding genes such as *Isg15*, *Ccl3*, and *Cd274* (gene encoding for programmed death-ligand 1 [PD-L1]). PD-L1 is expressed by activated neutrophils with lymphocyte suppressive capacities.[11,39] Our data show that, at 2 and 3 dpi, neutrophils and endothelial cells predominantly express *Cd274* while the expression of the corresponding receptor *Pdcd1* (gene encoding for programmed cell death protein 1 [PD-1]) is mainly confined to T and NK cells (Figure S4B). Specifically, expression analysis of *Cd274* in the neutrophil subset confirmed that upregulation is strongest in high-dose-infected Roborovski hamsters at 2 dpi (Figure S1C). Accordingly, expression analysis of *Pdcd1* in the T cell subset revealed that the PD-L1 receptor likewise had the highest expression in high-dose-infected Roborovski hamsters at that time point (Figure S1C). In agreement with these findings, our gene set enrichment analyses (Figures 4E and S4D) showed that ribosome-specific genes most strongly associated with lower DC1, indicating an initially high and further decreasing ribosomal activity of cells upon infection. In contrast, high DC1 was characterized by the enrichment of multiple proinflammatory and immunomodulatory pathways, including TNFα and interferon-mediated signaling. While inflammatory response scores increased with DC1 for all neutrophils (Figures 4F and S4E), those from high-dose-infected Roborovski hamsters extended furthest toward the right side of DC1, suggesting an overall higher inflammatory state and lymphocyte-suppressive capacity triggered in this species upon infection, matching observations made in severe COVID-19 patients.[11]
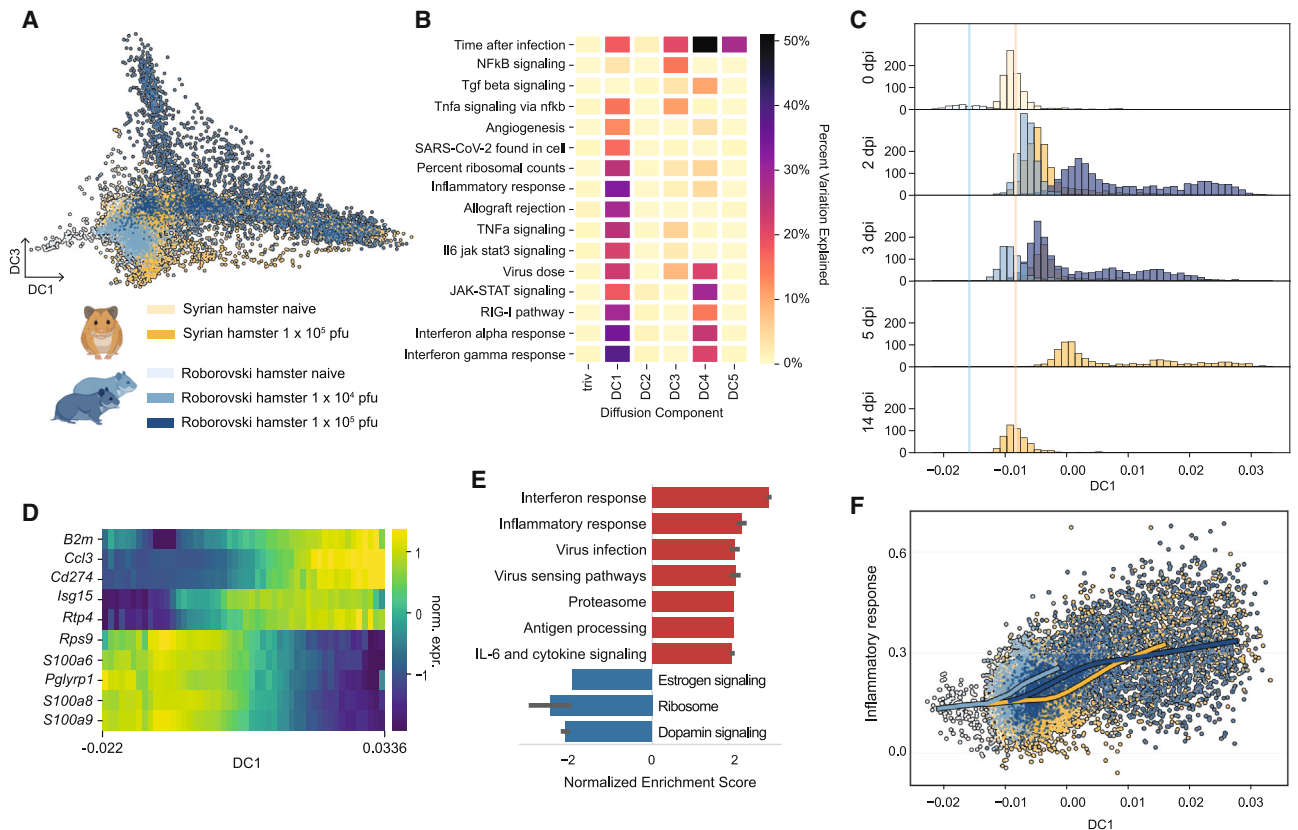
Figure 4. Factor analysis of neutrophils reveals a shared axis of inflammation

(A) Low-dimensional embedding of first and third diffusion component (DC) for all neutrophils, colored by hamster species and virus dose.

(B) Percentage variance explained by selected covariates for first five DCs.

(C) Distribution of neutrophils along DC1, split by dpi and colored by hamster species and virus dose as shown in (A). Mean position of uninfected cells per hamster type on DC1 is marked with a vertical line.

(D) Heatmap with gene expression trends for top five (anti-)correlating genes with DC1. Gene expression is Z score normalized and convolved by a uniform kernel across seven bins.

(E) Significant ($p < 0.05$) gene set groups from GSEA on genes ranked by correlation with DC1 showing the degree of enrichment in genes with higher positive or negative DC1 correlations. Data are represented as normalized enrichment scores across gene set clusters ± SD.

(F) Inflammatory response score of neutrophils along DC1 colored by hamster species and virus dose as shown in (A). Lines indicate locally estimated scatterplot smoothing (LOESS) regression along DC1.

Identification of a dominant inflammatory response program in endothelial cells

COVID-19 is also a vascular disease.[40] Nonetheless, endothelial cells, despite their likely importance in determining vascular vulnerability, remain understudied. Due to their limited accessibility, human endothelial cells have primarily been analyzed from postmortem lung tissues or *in vitro* systems. To fill this gap, we analyzed endothelial cells analogously to neutrophils. We used a diffusion map approach, followed by gene expression and gene set enrichment analyses to identify the molecular drivers that define characteristic DCs (Figures 5 and S5). While the first three DCs described endothelial cell subtype identities (primarily bronchial, vein, artery, and capillary) (Figures 5A and 5B), DC4 identified the dominant transcriptional program of endothelial cell responses to SARS-CoV-2 infection, as its variance was explained by a spectrum of proinflammatory pathways (Figure 5B), prompting us to study the dynamics and genes of this component in more detail.

As seen with neutrophils, endothelial cells were located on the lower/left end of DC4 before infection (0 dpi), but they shifted toward the right end of DC4 and took on different DC4 values upon infection (Figures 5C and S5A). In particular, bronchial and capillary endothelial cells from high-dose-infected Roborovski hamsters most rapidly increased in DC4 at 2 dpi before shifting slightly back at 3 dpi. Against this trend, endothelial cells from Syrian hamsters overall only mildly increased in DC4 throughout 2 and 3 dpi, peaking at 5 dpi, and entirely returned to the original state (0 dpi) at 14 dpi. Altogether, DC4 is an axis that was shared between hamster species and that, upon infection, was occupied much more rapidly and to a greater extent in high-dose-infected Roborovski while appearing to be transient in Syrian hamsters. Genes for which the expression correlated positively with increasing DC4 included numerous interferon-stimulated genes such as *Isg15*, *Rsad2*, and *Ifit2*, as well as chemokines *Cxcl10* and *Cxcl11* (Figures 5D and S5B), and showed significant upregulation ($p = 0$) of virus infection/sensing, TNF inflammation, and
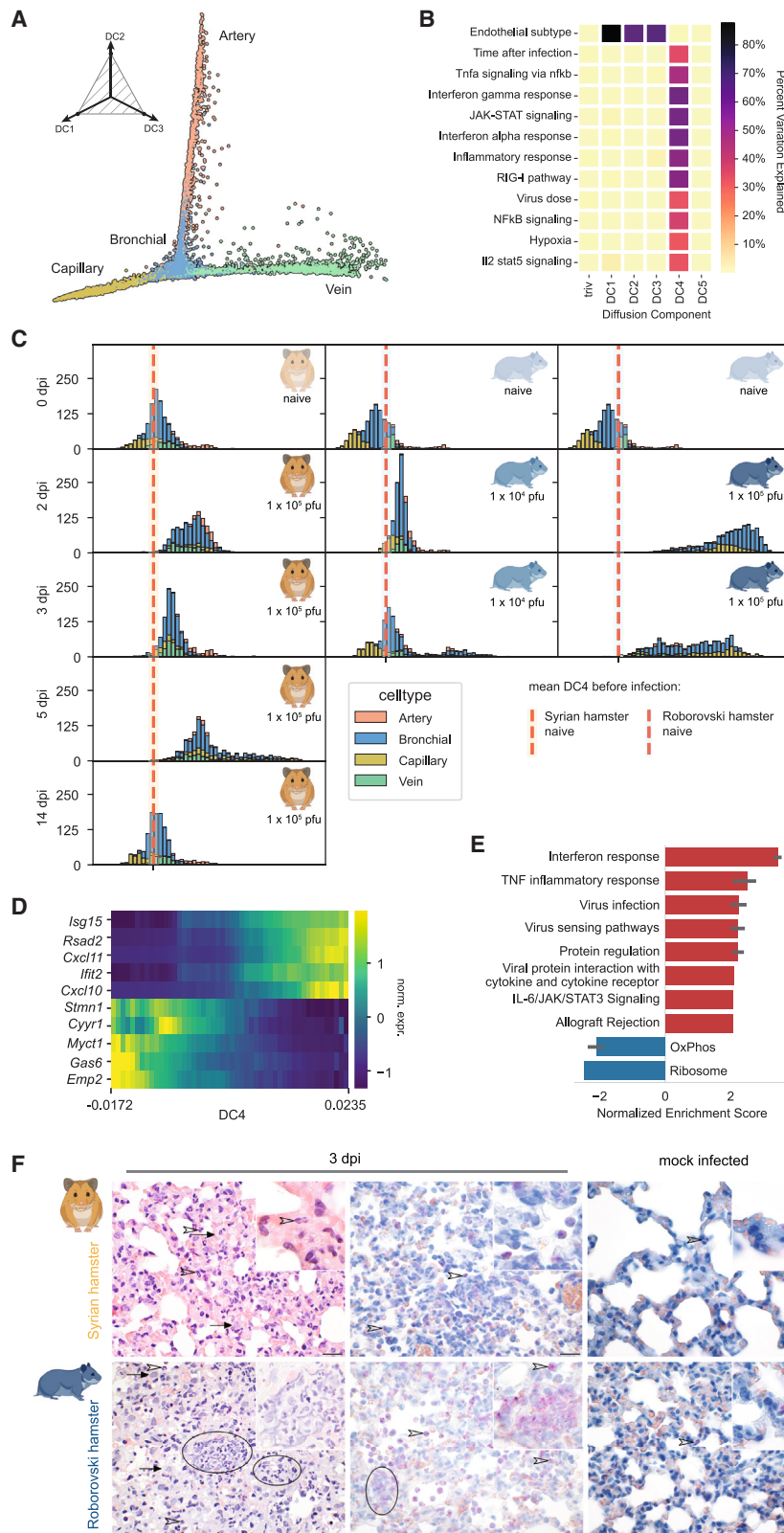
Figure 5. Endothelial cells transiently react to SARS-CoV-2 infection

(A) Simplex plot of the first three DCs for endothelial cells, colored by subtype.

(B) Variance explained by selected covariates for top five DCs.

(C) Distribution of cells along DC4, split vertically by hamster species and virus dose and horizontally by dpi, colored by endothelial cell subtype. Average value of DC4 for 0 dpi marked with red vertical line.

(D) Heatmap with gene expression trends for top five (anti-)correlating genes with DC4. Gene expression is Z score normalized and convolved by a uniform kernel across seven bins.

(E) Significant ($p < 0.05$) gene set groups for GSEA on genes ranked by correlation with DC4 showing the degree of enrichment in genes with higher positive or negative DC4 correlations. Data are represented as normalized enrichment scores across gene set clusters. Error bars indicate ± SD.

(F) Neutrophils depicted by H&E and naphthol AS-D chloroacetate esterase (NACE) stain in infected lungs of Syrian (top) and Roborovski (bottom) hamsters at 3 dpi. Histopathology visualizing reactive neutrophils (open arrowheads) and macrophages (arrows). Of note, only Roborovski hamsters developed karyolytic smears/necrotic karyoplasm consistent with alveolar wall and interalveolar blood vessel necrosis (ovals). H&E stain (left), NACE stain (middle and right); original magnification = 600-fold or 1,000-fold (inserts); scale bars, 20 μm; infection with 1×10^5 pfu SARS-CoV-2.

immune response pathways (Figures 5E and S5C). For the latter, endothelial cells from high-dose-infected Roborovski hamsters scored by far highest in inflammatory response (Figure S5D). While this clearly highlights DC4 as an axis-of-infection response, genes anti-correlating with progressing DC4 were not classically associated with inflammation and, as already observed for neutrophils, included ribosomal genes. Notably, among all cell types, ribosomal gene expression was consistently and most strongly downregulated in neutrophils and endothelial cells from high-dose-infected Roborovski hamsters (Figure S6A). Concomitantly, in these hamsters, apoptosis signatures were strongly upregulated in endothelial and epithelial cells at 2 dpi (Figure S6B). Histopathologically, the aforementioned vastly different reactions to the infection in different subtypes of endothelial cells were accompanied by interalveolar wall and blood vessel necrosis with multifocal distinct aggregates of karyolytic smears and cellular debris (Figure 5F). The larger, primarily venous, endothelial cells from lungs of both hamster species exhibited adhesion and extravasation of leukocytes from the blood as well as dents typical of endotheliitis in both hamster species at 3 dpi. However, interalveolar capillaries and bronchial endothelial cells, while mildly affected in Syrian hamsters, were strongly distressed by necrosis in Roborovski hamsters at 2 and 3 dpi, especially in the higher-dose group. These different reactions by endothelial subtype are also visible on DC4, where capillary endothelial cells, particularly from Roborovski hamsters, are much further on the right compared to arterial and venous subtypes.

DISCUSSION

Since the emergence of SARS-CoV-2, there has been an unparalleled global effort to characterize the virus and understand the clinical course of COVID-19. A variety of animal models and patient cohort data revealed details on mechanisms of pathogenesis,[14,41] immunity,[42,43] and response to therapy,[44] which greatly improved our understanding of the disease. Macroscopic risk factors for severe disease, such as age and specific comorbidities, have been identified,[45] and also some molecular aspects, such as interferon autoantibodies or human leukocyte antigen (HLA) genotype.[46–48] Still, the fundamental question of the initial cellular mechanisms that direct the path to mild, moderate, or severe disease remains unsolved. There are two key obstacles to answering this question using human lung patient data. Firstly, such data are not available for early time points post infection. Secondly, bronchoalveolar lavages, which represent the typical sampling method, cover soluble immune cells well but tissue cells only to a very limited extent.

In order to overcome these hurdles (i.e., to comparatively study moderate and severe disease at its very onset), we here probed published and previously unpublished scRNA-seq datasets from patients and two COVID-19 hamster models for correlates of disease severity. Syrian hamsters show a moderate course of COVID-19 with subsequent recovery, whereas Roborovski dwarf hamsters frequently succumb to severe disease.[18] scRNA-seq data allow for unbiased, transcriptome-wide investigations of cellular activation states at single-cell resolution. They can therefore provide a comprehensive overview of the cellular

processes happening in COVID-19. By combining this and sampling of animals with different disease severity, we aimed to investigate early processes in the disease that may lead to different outcomes.

In our analysis, Syrian hamsters displayed an efficient type 1 immune response, including NK cell and monocyte recruitment into lungs. This is in line with patient data describing that a moderate course of COVID-19 correlates with functional NK cells.[49] The same study found that augmented expression levels of transforming growth factor β (TGF-β) suppressed NK cells in their antiviral properties, fostering a severe disease course. Following their efficient, initial innate response, Syrian hamsters generally survived beyond 3 dpi and mounted effective T cell and neutralizing antibody responses against SARS-CoV-2,[19] which was not observed in Roborovski hamsters. This could mean that, in this severe-disease animal model, either humane endpoint criteria are reached before an efficient antiviral T and B cell response can develop or that the inability to initiate this response is one root cause for severe disease.

In contrast to Syrian hamsters, in which we observed clear upregulation of type 1 lineage-determining TFs *Tbx21* and *Eomes*, we did not observe upregulation of the type 3 lineage-determining TF *Rorc* in Roborovski hamsters. Similarly, *Stat3*, a TF in the interleukin (IL)-6, IL-21, and IL-23 signaling pathways for Th17 cells, was upregulated in Syrian but not Roborovski hamsters. However, presence of cytokines *Il6* and *Il23a*, as well as *Socs1*, together with the absence of type 1 and type 2 associated transcription patterns, indicates a type 3 response in Roborovski hamsters with severe disease course.

The cell population most strikingly related to severity of inflammation and disease in patients, as well as hamsters, are neutrophils. Neutrophils are the downstream effector cells of type 3 immunity, providing defense against extracellular pathogens, such as bacteria and fungi at epithelial barriers.[30] However, neutrophils are also associated with autoimmune disease and infection-triggered immunopathology.[30,50–53] The protective role of neutrophils and type 3 immunity against viral infections is limited to specific cases, e.g., herpes simplex virus 1 (HSV-1) infection of the cornea, rhinovirus infection, and influenza infection,[54–56] yet their presence in the lower respiratory tract correlates with disease severity, most prominently in the case of highly pathogenic avian influenza (HPAI) infection.[57–59] Notably, for specific influenza A virus (IAV) variants with increased pathogenicity, enhanced neutrophil recruitment along with NK cell inhibition could be linked to distinct viral proteins.[60] In the context of SARS-CoV-2 infection, Th17 cells and neutrophils have been associated with increased disease severity and immunopathology,[11,61] yet no viral protein mediator has been discovered. We suspect that differential composition of innate immune cell populations in uninfected lungs between Roborovski and Syrian hamsters can affect differential response kinetics and types. Nevertheless, using diffusion analysis, we identified a latent factor in neutrophils uniquely characterizing their response to the infection across both hamster species, which revealed an overly exacerbated pulmonary neutrophil response in Roborovski hamsters. Similar trends were observed when comparing blood neutrophils between Roborovski and Syrian hamsters.[62] Based on this finding, our data clearly link inflammatory neutrophils to

disease severity and align with previous studies in which we showed that dampening neutrophilic inflammation by dexamethasone treatment prevents lethal disease outcomes.[63] Moreover, inflammatory neutrophils in severely diseased Roborovski hamsters strongly expressed *Cd274*, as do human neutrophils in patients with a severe disease course.[61] However, the origin of the neutrophil response remains obscure. One putative mechanism could be enhanced virus-associated tissue damage in Roborovski hamsters resulting in enhanced release of DAMPs; increased activation of sensing receptors, such as Toll-like receptors (TLRs); and stronger release of downstream inflammatory mediators. Indeed, in histological lesions, we observed indications for enhanced necrosis in Roborovski hamsters as well as higher expression of *Il6*, which, together with TGF-β, is a type 3 immunity polarizing cytokine.

An important hallmark of COVID-19 pathogenesis is endothelial damage across multiple organs. Since endothelial cells are challenging to study in human patients, animal models may be of particular use. In our diffusion analysis, we identified an axis of inflammation (DC4), i.e., a specific gene expression program marked by upregulation of proinflammatory genes that endothelial cells follow upon infection. This effect was particularly strong for bronchial and capillary cells of high-dose-infected Roborovski hamsters. In the histopathological analysis, we observed endothelial cell necrosis, particularly in high-dose-infected Roborovski hamsters. Still, it is important to note that endothelial cells were also strongly activated along DC4 in Syrian hamsters, but they reverted to ground state and did not show obvious histological endothelial damage. It thus appears that endothelial activation is associated with disease severity, but this is not necessarily causative and, under beneficial conditions, is also reversible.

Our data from lung tissues offer a unique perspective on the involvement of endothelial cells in the pathological development of a severe disease course, given the lack of corresponding samples and data from humans. Notably, our findings suggest that immunological events early in the course of SARS-CoV-2 infection cause development of either type 1- or type 3-biased immune responses, thereby determining disease progression in both hamsters and humans. Future research can make use of the Roborovski hamster model for severe COVID-19-like disease to further elucidate mechanisms of severe disease and investigate potential medical interventions.

Limitations of the study

Our study provides an in-depth molecular characterization of biological processes in hamster lungs upon SARS-CoV-2-infection and identifies cell types and immunological programs that associate with different COVID-19 outcomes. Nevertheless, further investigation is needed to validate these findings and to fully decipher the pathophysiological mechanisms that are triggered by the virus. This particularly requires the use of complementary methods to link immune type and effector cells to disease severity. However, this is greatly limited by the lack of gene-knockout hamsters and depletion antibodies for both hamster species. Beyond the assay used, several limitations are imposed by the inaccessibility of specific samples. For instance, the lack of scRNA-seq data from SARS-CoV-2-in-fected pre-mortem human lung tissue precludes cross-species comparison of cell-specific features observed in endothelial cells and IMs, which we found to be highly responsive to infection. Finally, interventional studies on specific cell types in controlled environments are needed to robustly establish causality in pathogenesis.

STAR★METHODS

Detailed methods are provided in the online version of this paper and include the following:

- KEY RESOURCES TABLE
- RESOURCE AVAILABILITY
  - Lead contact
  - Materials availability
  - Data and code availability
- EXPERIMENTAL MODEL AND STUDY PARTICIPANT DETAILS
  - Animal husbandry
  - Cells and virus
- METHOD DETAILS
  - Animal experimentation
  - Single-cell isolation
  - Generation of single-cell RNA-sequencing data
  - Histopathology
- QUANTIFICATION AND STATISTICAL ANALYSIS
  - Processing of single-cell RNA-seq data
  - Filtering, clustering, and cell type annotation
  - Differential expression analysis
  - Mapping orthologous genes between hamster and human genomes
  - Integration of hamster data with scVI
  - Diffusion analysis of neutrophils and endothelial cells
  - Post-hoc interpretation of diffusion components
  - Gene set enrichment analysis
  - Selection criteria and processing of human SARS-CoV2 scRNA-seq counts

AUTHOR CONTRIBUTIONS

Conceptualization, S.P., G.N., E.W., M.W., J.T., M.L., and S.D.P.; methodology, S.P., G.N., P.P., E.W., J.T., and S.D.P.; investigation, S.P., G.N., E.W., J.M.A., S.K., A.V., J.K., F.P., P.P., D.P., L.G.T.A., A.D.G., J.T., M.L., and

REFERENCES

1. Michalski, J.E., Kurche, J.S., and Schwartz, D.A. (2022). From ARDS to pulmonary fibrosis: the next phase of the COVID-19 pandemic? Transl. Res. 241, 13–24. https://doi.org/10.1016/j.trsl.2021.09.001.

2. Mohammadi, A., Balan, I., Yadav, S., Matos, W.F., Kharawala, A., Gaddam, M., Sarabia, N., Koneru, S.C., Suddapalli, S.K., and Marzban, S. (2022). Post-COVID-19 Pulmonary Fibrosis. Cureus 14, e22770. https://doi.org/10.7759/cureus.22770.

3. Jasim, S.A., Mahdi, R.S., Bokov, D.O., Najm, M.A.A., Sobirova, G.N., Bafoyeva, Z.O., Taifi, A., Alkadir, O.K.A., Mustafa, Y.F., Mirzaei, R., and Karampoor, S. (2022). The deciphering of the immune cells and marker signature in COVID-19 pathogenesis: An update. J. Med. Virol. 94, 5128–5148. https://doi.org/10.1002/jmv.28000.

4. Knoll, R., Schultze, J.L., and Schulte-Schrepping, J. (2021). Monocytes and Macrophages in COVID-19. Front. Immunol. 12, 720109. https://doi.org/10.3389/fimmu.2021.720109.

5. Vora, S.M., Lieberman, J., and Wu, H. (2021). Inflammasome activation at the crux of severe COVID-19. Nat. Rev. Immunol. 21, 694–703. https://doi.org/10.1038/s41577-021-00588-x.

6. Castanheira, F.V.S., and Kubes, P. (2023). Neutrophils during SARS-CoV-2 infection: Friend or foe? Immunol. Rev. 314, 399–412. https://doi.org/10.1111/imr.13175.

7. Paludan, S.R., and Mogensen, T.H. (2022). Innate immunological pathways in COVID-19 pathogenesis. Sci. Immunol. 7, eabm5505. https://doi.org/10.1126/sciimmunol.abm5505.

8. Hernandez Acosta, R.A., Esquer Garrigos, Z., Marcelin, J.R., and Vijayvargiya, P. (2022). COVID-19 Pathogenesis and Clinical Manifestations. Infect. Dis. Clin. North Am. 36, 231–249. https://doi.org/10.1016/j.idc.2022.01.003.

9. Remy, K.E., Mazer, M., Striker, D.A., Ellebedy, A.H., Walton, A.H., Unsinger, J., Blood, T.M., Mudd, P.A., Yi, D.J., Mannion, D.A., et al. (2020). Severe immunosuppression and not a cytokine storm characterizes COVID-19 infections. JCI Insight 5, e140329. https://doi.org/10.1172/jci.insight.140329.

10. Wendisch, D., Dietrich, O., Mari, T., Von Stillfried, S., Ibarra, I.L., Mittermaier, M., Mache, C., Chua, R.L., Knoll, R., Timm, S., et al. (2021). SARS-CoV-2 infection triggers profibrotic macrophage responses and lung fibrosis. Cell 184, 6243–6261.e27. https://doi.org/10.1016/j.cell.2021.11.033.

11. Schulte-Schrepping, J., Reusch, N., Paclik, D., Baßler, K., Schlickeiser, S., Zhang, B., Krämer, B., Krammer, T., Brumhard, S., Bonaguro, L., et al. (2020). Severe COVID-19 Is Marked by a Dysregulated Myeloid Cell Compartment. Cell 182, 1419–1440.e23. https://doi.org/10.1016/j.cell.2020.08.001.

12. Falcinelli, E., Petito, E., and Gresele, P. (2022). The role of platelets, neutrophils and endothelium in COVID-19 infection. Expert Rev. Hematol. 15, 727–745. https://doi.org/10.1080/17474086.2022.2110061.

13. Zhang, R., Sun, C., Han, Y., Huang, L., Sheng, H., Wang, J., Zhang, Y., Lai, J., Yuan, J., Chen, X., et al. (2023). Neutrophil autophagy and NETosis in COVID-19: perspectives. Autophagy 19, 758–767. https://doi.org/10.1080/15548627.2022.2099206.

14. Fan, C., Wu, Y., Rui, X., Yang, Y., Ling, C., Liu, S., Liu, S., and Wang, Y. (2022). Animal models for COVID-19: advances, gaps and perspectives. Signal Transduct. Target. Ther. 7, 220. https://doi.org/10.1038/s41392-022-01087-8.

15. Qi, F., and Qin, C. (2022). Characteristics of animal models for COVID-19. Animal Model. Exp. Med. 5, 401–409. https://doi.org/10.1002/ame2.12278.

16. Gruber, A.D., Firsching, T.C., Trimpert, J., and Dietert, K. (2022). Hamster models of COVID-19 pneumonia reviewed: How human can they be? Vet. Pathol. 59, 528–545. https://doi.org/10.1177/03009858211057197.

17. Chu, H., Chan, J.F.W., and Yuen, K.Y. (2022). Animal models in SARS-CoV-2 research. Nat. Methods 19, 392–394. https://doi.org/10.1038/s41592-022-01447-w.

18. Trimpert, J., Vladimirova, D., Dietert, K., Abdelgawad, A., Kunec, D., Dökel, S., Voss, A., Gruber, A.D., Bertzbach, L.D., and Osterrieder, N. (2020). The Roborovski Dwarf Hamster Is A Highly Susceptible Model for a Rapid and Fatal Course of SARS-CoV-2 Infection. Cell Rep. 33, 108488. https://doi.org/10.1016/j.celrep.2020.108488.

19. Nouailles, G., Wyler, E., Pennitz, P., Postmus, D., Vladimirova, D., Kazmierski, J., Pott, F., Dietert, K., Muelleder, M., Farztdinov, V., et al. (2021). Temporal omics analysis in Syrian hamsters unravel cellular effector responses to moderate COVID-19. Nat. Commun. 12, 4869. https://doi.org/10.1038/s41467-021-25030-7.

20. Chua, R.L., Lukassen, S., Trump, S., Hennig, B.P., Wendisch, D., Pott, F., Debnath, O., Thürmann, L., Kurth, F., Völker, M.T., et al. (2020). COVID-19 severity correlates with airway epithelium–immune cell interactions identified by single-cell analysis. Nat. Biotechnol. 38, 970–979. https://doi.org/10.1038/s41587-020-0602-4.

21. Liao, M., Liu, Y., Yuan, J., Wen, Y., Xu, G., Zhao, J., Cheng, L., Li, J., Wang, X., Wang, F., et al. (2020). Single-cell landscape of bronchoalveolar immune cells in patients with COVID-19. Nat. Med. 26, 842–844. https://doi.org/10.1038/s41591-020-0901-9.

22. Melms, J.C., Biermann, J., Huang, H., Wang, Y., Nair, A., Tagore, S., Katsyv, I., Rendeiro, A.F., Amin, A.D., Schapiro, D., et al. (2021). A molecular single-cell lung atlas of lethal COVID-19. Nature 595, 114–119. https://doi.org/10.1038/s41586-021-03569-1.

23. Subramanian, A., Tamayo, P., Mootha, V.K., Mukherjee, S., Ebert, B.L., Gillette, M.A., Paulovich, A., Pomeroy, S.L., Golub, T.R., Lander, E.S., and Mesirov, J.P. (2005). Gene set enrichment analysis: A knowledge-based approach for interpreting genome-wide expression profiles. Proc. Natl. Acad. Sci. USA 102, 15545–15550. https://doi.org/10.1073/pnas.0506580102.

24. Kanehisa, M., and Goto, S. (2000). KEGG: Kyoto Encyclopedia of Genes and Genomes. Nucleic Acids Res. 28, 27–30. https://doi.org/10.1093/nar/28.1.27.

25. Kanehisa, M. (2019). Toward understanding the origin and evolution of cellular organisms. Protein Sci. 28, 1947–1951. https://doi.org/10.1002/pro.3715.

26. Kanehisa, M., Furumichi, M., Sato, Y., Kawashima, M., and Ishiguro-Watanabe, M. (2023). KEGG for taxonomy-based analysis of pathways and genomes. Nucleic Acids Res. 51, D587-d592. https://doi.org/10.1093/nar/gkac963.

27. Liberzon, A., Birger, C., Thorvaldsdóttir, H., Ghandi, M., Mesirov, J.P., and Tamayo, P. (2015). The Molecular Signatures Database (MSigDB) hallmark gene set collection. Cell Syst. 1, 417–425. https://doi.org/10.1016/j.cels.2015.12.004.

28. Osterrieder, N., Bertzbach, L.D., Dietert, K., Abdelgawad, A., Vladimirova, D., Kunec, D., Hoffmann, D., Beer, M., Gruber, A.D., and Trimpert, J.

(2020). Age-Dependent Progression of SARS-CoV-2 Infection in Syrian Hamsters. Viruses *12*, 779. https://doi.org/10.3390/v12070779.

29. Hou, Y.J., Okuda, K., Edwards, C.E., Martinez, D.R., Asakura, T., Dinnon, K.H., 3rd, Kato, T., Lee, R.E., Yount, B.L., Mascenik, T.M., et al. (2020). SARS-CoV-2 Reverse Genetics Reveals a Variable Infection Gradient in the Respiratory Tract. Cell *182*, 429–446.e14. https://doi.org/10.1016/j.cell.2020.05.042.

30. Annunziato, F., Romagnani, C., and Romagnani, S. (2015). The 3 major types of innate and adaptive cell-mediated effector immunity. J. Allergy Clin. Immunol. *135*, 626–635. https://doi.org/10.1016/j.jaci.2014.11.001.

31. Zhang, J., Le Gras, S., Pouxvielh, K., Faure, F., Fallone, L., Kern, N., Moreews, M., Mathieu, A.L., Schneider, R., Marliac, Q., et al. (2021). Sequential actions of EOMES and T-BET promote stepwise maturation of natural killer cells. Nat. Commun. *12*, 5446. https://doi.org/10.1038/s41467-021-25758-2.

32. Zhou, L. (2012). Striking similarity: GATA-3 regulates ILC2 and Th2 cells. Immunity *37*, 589–591. https://doi.org/10.1016/j.immuni.2012.10.002.

33. Song, H., Suehiro, J.i., Kanki, Y., Kawai, Y., Inoue, K., Daida, H., Yano, K., Ohhashi, T., Oettgen, P., Aird, W.C., et al. (2009). Critical role for GATA3 in mediating Tie2 expression and function in large vessel endothelial cells. J. Biol. Chem. *284*, 29109–29124. https://doi.org/10.1074/jbc.M109.041145.

34. Sobah, M.L., Liongue, C., and Ward, A.C. (2021). SOCS Proteins in Immunity, Inflammatory Diseases, and Immune-Related Cancer. Front. Med. *8*, 727987. https://doi.org/10.3389/fmed.2021.727987.

35. Coifman, R.R., and Lafon, S. (2006). Diffusion maps. Appl. Comput. Harmon. Anal. *21*, 5–30. https://doi.org/10.1016/j.acha.2006.04.006.

36. Haghverdi, L., Buettner, F., and Theis, F.J. (2015). Diffusion maps for high-dimensional single-cell analysis of differentiation data. Bioinformatics *31*, 2989–2998. https://doi.org/10.1093/bioinformatics/btv325.

37. Wang, S., Song, R., Wang, Z., Jing, Z., Wang, S., and Ma, J. (2018). S100A8/A9 in Inflammation. Front. Immunol. *9*, 1298. https://doi.org/10.3389/fimmu.2018.01298.

38. Sprenkeler, E.G.G., Zandstra, J., van Kleef, N.D., Goetschalckx, I., Verstegen, B., Aarts, C.E.M., Janssen, H., Tool, A.T.J., van Mierlo, G., van Bruggen, R., et al. (2022). S100A8/A9 Is a Marker for the Release of Neutrophil Extracellular Traps and Induces Neutrophil Activation. Cells *11*, 236. https://doi.org/10.3390/cells11020236.

39. de Kleijn, S., Langereis, J.D., Leentjens, J., Kox, M., Netea, M.G., Koenderman, L., Ferwerda, G., Pickkers, P., and Hermans, P.W.M. (2013). IFN-γ-stimulated neutrophils suppress lymphocyte proliferation through expression of PD-L1. PLoS One *8*, e72249. https://doi.org/10.1371/journal.pone.0072249.

40. Siddiqi, H.K., Libby, P., and Ridker, P.M. (2021). COVID-19 - A vascular disease. Trends Cardiovasc. Med. *31*, 1–5. https://doi.org/10.1016/j.tcm.2020.10.005.

41. Choudhary, S., Kanevsky, I., and Tomlinson, L. (2022). Animal models for studying COVID-19, prevention, and therapy: Pathology and disease phenotypes. Vet. Pathol. *59*, 516–527. https://doi.org/10.1177/03009858221092015.

42. Brady, C., Tipton, T., Longet, S., and Carroll, M.W. (2023). Pre-clinical models to define correlates of protection for SARS-CoV-2. Front. Immunol. *14*, 1166664. https://doi.org/10.3389/fimmu.2023.1166664.

43. Clever, S., and Volz, A. (2023). Mouse models in COVID-19 research: analyzing the adaptive immune response. Med. Microbiol. Immunol. *212*, 165–183. https://doi.org/10.1007/s00430-022-00735-8.

44. Li, G., Hilgenfeld, R., Whitley, R., and De Clercq, E. (2023). Therapeutic strategies for COVID-19: progress and lessons learned. Nat. Rev. Drug Discov. *22*, 449–475. https://doi.org/10.1038/s41573-023-00672-y.

45. Gao, Y.D., Ding, M., Dong, X., Zhang, J.J., Kursat Azkur, A., Azkur, D., Gan, H., Sun, Y.L., Fu, W., Li, W., et al. (2021). Risk factors for severe and critically ill COVID-19 patients: A review. Allergy *76*, 428–455. https://doi.org/10.1111/all.14657.

46. Zhang, Q., Bastard, P., COVID Human Genetic Effort; Cobat, A., and Casanova, J.L. (2022). Human genetic and immunological determinants of critical COVID-19 pneumonia. Nature *603*, 587–598. https://doi.org/10.1038/s41586-022-04447-0.

47. Garmendia, J.V., García, A.H., De Sanctis, C.V., Hajdúch, M., and De Sanctis, J.B. (2022). Autoimmunity and Immunodeficiency in Severe SARS-CoV-2 Infection and Prolonged COVID-19. Curr. Issues Mol. Biol. *45*, 33–50. https://doi.org/10.3390/cimb45010003.

48. Augusto, D.G., Murdolo, L.D., Chatzileontiadou, D.S.M., Sabatino, J.J., Jr., Yusufali, T., Peyser, N.D., Butcher, X., Kizer, K., Guthrie, K., Murray, V.W., et al. (2023). A common allele of HLA is associated with asymptomatic SARS-CoV-2 infection. Nature *620*, 128–136. https://doi.org/10.1038/s41586-023-06331-x.

49. Witkowski, M., Tizian, C., Ferreira-Gomes, M., Niemeyer, D., Jones, T.C., Heinrich, F., Frischbutter, S., Angermair, S., Hohnstein, T., Mattiola, I., et al. (2021). Untimely TGFβ responses in COVID-19 limit antiviral functions of NK cells. Nature *600*, 295–301. https://doi.org/10.1038/s41586-021-04142-6.

50. Saleh, M.M., and Petri, W.A., Jr. (2019). Type 3 Immunity during Clostridioides difficile Infection: Too Much of a Good Thing? Infect. Immun. *88*, e00306-19. https://doi.org/10.1128/iai.00306-19.

51. Borkner, L., Curham, L.M., Wilk, M.M., Moran, B., and Mills, K.H.G. (2021). IL-17 mediates protective immunity against nasal infection with Bordetella pertussis by mobilizing neutrophils, especially Siglec-F(+) neutrophils. Mucosal Immunol. *14*, 1183–1202. https://doi.org/10.1038/s41385-021-00407-5.

52. Lu, Y.J., Gross, J., Bogaert, D., Finn, A., Bagrade, L., Zhang, Q., Kolls, J.K., Srivastava, A., Lundgren, A., Forte, S., et al. (2008). Interleukin-17A mediates acquired immunity to pneumococcal colonization. PLoS Pathog. *4*, e1000159. https://doi.org/10.1371/journal.ppat.1000159.

53. Zheng, Y., Danilenko, D.M., Valdez, P., Kasman, I., Eastham-Anderson, J., Wu, J., and Ouyang, W. (2007). Interleukin-22, a T(H)17 cytokine, mediates IL-23-induced dermal inflammation and acanthosis. Nature *445*, 648–651. https://doi.org/10.1038/nature05505.

54. Kim, B., Sarangi, P.P., Azkur, A.K., Kaistha, S.D., and Rouse, B.T. (2008). Enhanced viral immunoinflammatory lesions in mice lacking IL-23 responses. Microbes Infect. *10*, 302–312. https://doi.org/10.1016/j.micinf.2007.12.007.

55. Wiehler, S., and Proud, D. (2007). Interleukin-17A modulates human airway epithelial responses to human rhinovirus infection. Am. J. Physiol. Lung Cell Mol. Physiol. *293*, L505–L515. https://doi.org/10.1152/ajplung.00066.2007.

56. Hamada, H., Garcia-Hernandez, M.d.l.L., Reome, J.B., Misra, S.K., Strutt, T.M., McKinstry, K.K., Cooper, A.M., Swain, S.L., and Dutton, R.W. (2009). Tc17, a unique subset of CD8 T cells that can protect against lethal influenza challenge. J. Immunol. *182*, 3469–3481. https://doi.org/10.4049/jimmunol.0801814.

57. Camp, J.V., and Jonsson, C.B. (2017). A Role for Neutrophils in Viral Respiratory Disease. Front. Immunol. *8*, 550. https://doi.org/10.3389/fimmu.2017.00550.

58. Laghlali, G., Lawlor, K.E., and Tate, M.D. (2020). Die Another Way: Interplay between Influenza A Virus, Inflammation and Cell Death. Viruses *12*, 401. https://doi.org/10.3390/v12040401.

59. Tate, M.D., Ioannidis, L.J., Croker, B., Brown, L.E., Brooks, A.G., and Reading, P.C. (2011). The role of neutrophils during mild and severe influenza virus infections of mice. PLoS One *6*, e17618. https://doi.org/10.1371/journal.pone.0017618.

60. Vidy, A., Maisonnasse, P., Da Costa, B., Delmas, B., Chevalier, C., and Le Goffic, R. (2016). The Influenza Virus Protein PB1-F2 Increases Viral Pathogenesis through Neutrophil Recruitment and NK Cells Inhibition. PLoS One *11*, e0165361. https://doi.org/10.1371/journal.pone.0165361.

61. Orlov, M., Wander, P.L., Morrell, E.D., Mikacenic, C., and Wurfel, M.M. (2020). A Case for Targeting Th17 Cells and IL-17A in SARS-CoV-2

Infections. J. Immunol. *205*, 892–898. https://doi.org/10.4049/jimmu-nol.2000554.

62. Friedrich, V.D., Pennitz, P., Wyler, E., Adler, J.M., Postmus, D., Alves, L.G.T., Prigann, J., Pott, F., Vladimirova, D., Hoefler, T., et al. (2024). Neural Network-Assisted Humanization of COVID-19 Hamster scRNAseq Data Reveals Matching Severity States in Human Disease. Preprint at bioRxiv. https://doi.org/10.1101/2024.01.11.574849.

63. Wyler, E., Adler, J.M., Eschke, K., Teixeira Alves, G., Peidli, S., Pott, F., Kazmierski, J., Michalick, L., Kershaw, O., Bushe, J., et al. (2022). Key benefits of dexamethasone and antibody treatment in COVID-19 hamster models revealed by single-cell transcriptomics. Mol. Ther. *30*, 1952–1965. https://doi.org/10.1016/j.ymthe.2022.03.014.

64. Wölfel, R., Corman, V.M., Guggemos, W., Seilmaier, M., Zange, S., Müller, M.A., Niemeyer, D., Jones, T.C., Vollmar, P., Rothe, C., et al. (2020). Virological assessment of hospitalized patients with COVID-2019. Nature *581*, 465–469. https://doi.org/10.1038/s41586-020-2196-x.

65. Andreotti, S., Altmüller, J., Quedenau, C., Borodina, T., Nouailles, G., Teixeira Alves, L.G., Landthaler, M., Bieniara, M., Trimpert, J., and Wyler, E. (2022). De Novo-Whole Genome Assembly of the Roborovski Dwarf Hamster (Phodopus roborovskii) Genome: An Animal Model for Severe/Critical COVID-19. Genome Biol Evol *14*, evac100. https://doi.org/10.1093/gbe/evac100.

66. Nouailles, G., Adler, J.M., Pennitz, P., Peidli, S., Teixeira Alves, L.G., Baumgardt, M., Bushe, J., Voss, A., Langenhagen, A., Langner, C., et al. (2023). Live-attenuated vaccine sCPD9 elicits superior mucosal and systemic immunity to SARS-CoV-2 variants in hamsters. Nat. Microbiol. *8*, 860–874. https://doi.org/10.1038/s41564-023-01352-8.

67. Smedley, D., Haider, S., Ballester, B., Holland, R., London, D., Thorisson, G., and Kasprzyk, A. (2009). BioMart – biological queries made easy. BMC Genom. *10*, 22. https://doi.org/10.1186/1471-2164-10-22.

68. Schubert, M., Klinger, B., Klünemann, M., Sieber, A., Uhlitz, F., Sauer, S., Garnett, M.J., Blüthgen, N., and Saez-Rodriguez, J. (2018). Perturbation-response genes reveal signaling footprints in cancer gene expression. Nat. Commun. *9*, 20. https://doi.org/10.1038/s41467-017-02391-6.

69. Corman, V.M., Landt, O., Kaiser, M., Molenkamp, R., Meijer, A., Chu, D.K., Bleicker, T., Brünink, S., Schneider, J., Schmidt, M.L., et al. (2020). Detection of 2019 novel coronavirus (2019-nCoV) by real-time RT-PCR. Euro Surveill. *25*, 2000045. https://doi.org/10.2807/1560-7917.ES.2020.25.3.2000045.

70. Wolf, F.A., Angerer, P., and Theis, F.J. (2018). SCANPY: large-scale single-cell gene expression data analysis. Genome Biol. *19*, 15. https://doi.org/10.1186/s13059-017-1382-0.

71. Love, M.I., Huber, W., and Anders, S. (2014). Moderated estimation of fold change and dispersion for RNA-seq data with DESeq2. Genome Biol. *15*, 550. https://doi.org/10.1186/s13059-014-0550-8.

72. Lopez, R., Regier, J., Cole, M.B., Jordan, M.I., and Yosef, N. (2018). Deep generative modeling for single-cell transcriptomics. Nat. Methods *15*, 1053–1058. https://doi.org/10.1038/s41592-018-0229-2.

73. Satija, R., Farrell, J.A., Gennert, D., Schier, A.F., and Regev, A. (2015). Spatial reconstruction of single-cell gene expression data. Nat. Biotechnol. *33*, 495–502. https://doi.org/10.1038/nbt.3192.

74. Fang, Z., Liu, X., and Peltz, G. (2023). GSEApy: a comprehensive package for performing gene set enrichment analysis in Python. Bioinformatics *39*, btac757. https://doi.org/10.1093/bioinformatics/btac757.

75. Wolock, S.L., Lopez, R., and Klein, A.M. (2019). Scrublet: Computational Identification of Cell Doublets in Single-Cell Transcriptomic Data. Cell Syst. *8*, 281–291.e9. https://doi.org/10.1016/j.cels.2018.11.005.

76. Mölder, F., Jablonski, K.P., Letcher, B., Hall, M.B., Tomkins-Tinch, C.H., Sochat, V., Forster, J., Lee, S., Twardziok, S.O., Kanitz, A., et al. (2021). Sustainable data analysis with Snakemake. F1000Res. *10*, 33. https://doi.org/10.12688/f1000research.29032.2.

77. Trimpert, J., Adler, J.M., Eschke, K., Abdelgawad, A., Firsching, T.C., Ebert, N., Thao, T.T.N., Gruber, A.D., Thiel, V., Osterrieder, N., and Kunec, D. (2021). Live attenuated virus vaccine protects against SARS-CoV-2 variants of concern B.1.1.7 (Alpha) and B.1.351 (Beta). Sci. Adv. *7*, eabk0172. https://doi.org/10.1126/sciadv.abk0172.

78. Adler, J.M., Martin Vidal, R., Voß, A., Kunder, S., Nascimento, M., Abdelgawad, A., Langner, C., Vladimirova, D., Osterrieder, N., Gruber, A.D., et al. (2023). A non-transmissible live attenuated SARS-CoV-2 vaccine. Mol. Ther. https://doi.org/10.1016/j.ymthe.2023.05.004.

79. Trimpert, J., Dietert, K., Firsching, T.C., Ebert, N., Thi Nhu Thao, T., Vladimirova, D., Kaufer, S., Labroussaa, F., Abdelgawad, A., Conradie, A., et al. (2021). Development of safe and highly protective live-attenuated SARS-CoV-2 vaccine candidates by genome recoding. Cell Rep. *36*, 109493. https://doi.org/10.1016/j.celrep.2021.109493.

80. Dietert, K., Gutbier, B., Wienhold, S.M., Reppe, K., Jiang, X., Yao, L., Chaput, C., Naujoks, J., Brack, M., Kupke, A., et al. (2017). Spectrum of pathogen- and model-specific histopathologies in mouse models of acute pneumonia. PLoS One *12*, e0188251. https://doi.org/10.1371/journal.pone.0188251.

81. McInnes, L., Healy, J., and Melville, J. (2020). UMAP: Uniform Manifold Approximation and Projection for Dimension Reduction. Preprint at arXiv. https://doi.org/10.48550/arXiv.1802.03426.

82. Hafemeister, C., and Satija, R. (2019). Normalization and variance stabilization of single-cell RNA-seq data using regularized negative binomial regression. Genome Biol. *20*, 296. https://doi.org/10.1186/s13059-019-1874-1.

83. Stuart, T., Butler, A., Hoffman, P., Hafemeister, C., Papalexi, E., Mauck, W.M., Hao, Y., Stoeckius, M., Smibert, P., and Satija, R. (2019). Comprehensive Integration of Single-Cell Data. Cell *177*, 1888–1902.e21. https://doi.org/10.1016/j.cell.2019.05.031.

84. Einstein, A. (1956). Investigations on the Theory of the Brownian Movement (Dover Publications).

85. Gardiner, C. (2009). Stochastic Methods: A Handbook for the Natural and Social Sciences (Springer Berlin Heidelberg).

Cell Reports
Article

STAR★METHODS

KEY RESOURCES TABLE

REAGENT or RESOURCE	SOURCE	IDENTIFIER
Bacterial and virus strains		
SARS-CoV-2	Wölfel et al.[64]	BetaCoV/Germany/BavPat1/2020
Biological samples		
Hamster lungs	This paper	N/A
Chemicals, peptides, and recombinant proteins		
Dispase	Corning	Cat#354235
DNAse	AppliChem	Cat#A3778,0100
Collagenase B	Roche	Cat#11088815001
Actinomycin D	Sigma-Aldrich	Cat#A9415-5MG
RBC Lysis buffer	Santa Cruz Biotechnology	Cat#sc-296258
Critical commercial assays		
Chromium Next Gem Chip G Single Cell Kit	10x Genomics	Cat#1000121
Chromium Next Gem Single cell 3' GEM, Library & Gel Bead Kit v3.1	10x Genomics	Cat#1000120
NEB Luna Universal Probe One-Step RT-qPCR kit	New England Biolabs	E3006L
innuPREP Virus RNA kit	Analytik Jena	Cat# 845-KS-4700250
Naphthol AS-D chloroacetate esterase (NACE) kit	Sigma-Aldrich	91C-1KT
Deposited data		
Roborovski hamster: scRNA-seq data from lung tissue of naive and SARS-CoV-2-infected animals	This paper	GEO: GSE241133
Source tables	This paper	https://doi.org/10.5281/zenodo.11124622
Syrian hamster: scRNA-seq data from lung tissue of naive and SARS-CoV-2-infected animals	Nouailles et al.[19]	GEO: GSE162208
Human nasal swab scRNA-seq data	Chua et al.[20]	https://doi.org/10.6084/m9.figshare.12436517.v2
Human BAL-fluid scRNA-seq data	Liao et al.[21]	GEO: GSE145926
Human postmortem lung tissue scRNA-seq data	Melms et al.[22]	GEO: GSE171524 and https://singlecell.broadinstitute.org/single_cell/study/SCP1219
Roborovski hamster genome	Andreotti et al.[65]	https://doi.org/10.6084/m9.figshare.16695457
Syrian hamster genome	Nouailles et al.[66]	GEO: GSE200596
Human-mouse orthologs	Smedley et al.[67]	https://www.ensembl.org/info/data/biomart/index.html
KEGG gene sets	Kanehisa et al.[25]	KEGG_2021_Human
MSigDB Hallmark gene sets	Liberzon et al.[27]	MSigDB_Hallmark_2020
PROGENy gene signatures	Schubert et al.[68]	https://doi.org/10.1038/s41467-017-02391-6
Experimental models: Cell lines		
African green monkey: Vero E6 cells	ATCC	CRL-1586
Experimental models: Organisms/strains		
Hamster: Syrian golden hamster (Mesocricetus auratus); RjHan:AURA	Janvier labs	N/A
Hamster: Roborovski hamster (Phodopus roborovskii)	German pet trade	N/A
Oligonucleotides		
RT-qPCR primers and probe	Corman et al.[69]	N/A

Continued

REAGENT or RESOURCE	SOURCE	IDENTIFIER
Synthetic probes for the in situ-detection of the nucleocapsid RNA of SARS-CoV-2 (NCBI database NC_045512.2, nucleotides 28,274 to 29,533)	Thermo Fisher Scientific	assay ID: VPNKRHM
Software and algorithms		
Code to reproduce analyses in this paper	This paper	https://github.com/stefanpeidli/PanCov19_Hamster; https://doi.org/10.5281/zenodo.11124622
Scanpy 1.9.1	Wolf et al.[70]	https://github.com/scverse/scanpy
DESeq2 1.38.3	Love et al.[71]	https://bioconductor.org/packages/release/bioc/html/DESeq2.html
Scvi-tools 0.19.0	Lopez et al.[72]	https://github.com/scverse/scvi-tools
CellRanger 6.1.1	10x Genomics	https://github.com/10XGenomics/cellranger
Seurat 4.0.6	Satija et al.[73]	https://github.com/satijalab/seurat
Gseapy 0.10.8	Fang et al.[74]	https://github.com/zqfang/GSEApy
Scrublet 0.2.3	Wolock et al.[75]	https://github.com/swolock/scrublet
Snakemake 7.20.0	Mölder et al.[76]	https://github.com/snakemake/snakemake
Prism 9.2.0	GraphPad Software	http://www.graphpad.com
cellSensTM Imaging Software 1.18	Olympus Soft Imaging Solutions	https://www.olympus-lifescience.com/en/software/cellsens/
Las X Stellaris software	Leica, Germany	https://www.leica-microsystems.com/products/microscope-software/p/leica-las-x-ls/
Other		
2100 Bioanalyzer Instrument	Agilent Technologies	Part#G2939BA
NovaSeq 6000	Illumina	Cat#20013850
NextSeq 550	Illumina	Cat#SY-415-1002
Chromium Controller	10x Genomics	Prod#1000204
Olympus BX41 microscope	Olympus, Hamburg, Germany	N/A
DP80 Microscope Digital Camera	Olympus, Hamburg, Germany	N/A
Inverse microscope DMi8 CS Premium (Stellaris 8 FALCON)	Leica Camera, Germany	N/A

RESOURCE AVAILABILITY

Lead contact
Further information and requests for resources and reagents should be directed to the lead contact, Samantha Praktiknjo (samantha.praktiknjo@bih-charite.de).

Materials availability
This study did not generate new unique reagents.

Data and code availability
- Single-cell RNA-seq data have been deposited at the Gene Expression Omnibus (GEO: GSE241133) and are publicly available as of the date of publication.
- This paper also analyzes existing, publicly available data. These accession numbers for the datasets are listed in the key resources table.
- Code for data analyses is available at GitHub (https://github.com/stefanpeidli/PanCov19_Hamster).
- Any additional information required to reanalyze the data reported in this paper is available from the lead contact upon request.

EXPERIMENTAL MODEL AND STUDY PARTICIPANT DETAILS

Animal husbandry

The animal experiments were approved by the competent state authority (Landesamt für Gesundheit und Soziales Berlin, Germany, approval number 0086/20) and were performed in accordance with national and international regulations. In accordance with the 3R principle, no additional animal experiments were performed for this study. Instead, we used data and samples from animals studied in our previously published research.[18,19,28] In these experiments, female and male Syrian hamsters (*Mesocricetus auratus*; RjHan:AURA, Janvier Labs, Saint-Berthevin, France) and Roborovski hamsters (*Phodopus roborovskii*, German pet trade) were housed in a BSL-3 facility in individually ventilated cages (IVCs; Tecniplast, Buguggiate, Italy) with abundant enrichment (Carfil, Oud-Turnhout, Belgium) and *ad libidum* access to food and water. Cage temperature and relative humidity were recorded daily and ranged from 22°C to 24°C and 40 to 55%, respectively. Animals were allowed at least 7 days to acclimatize before the start of the experiments.

Cells and virus

The SARS-CoV-2 isolate (BetaCoV/Germany/BavPat1/2020)[64] was kindly provided by Drs. Daniela Niemeyer and Christian Drosten, Charité Berlin, Germany. Virus stocks for animal experiments were obtained by propagating the virus under BSL-3 conditions on Vero E6 cells (ATCC CRL-1586) in minimal essential medium (MEM; PAN Biotech, Aidenbach, Germany) supplemented with 10% fetal bovine serum (FBS; PAN Biotech, Aidenbach, Germany), 100 IU/mL penicillin G, and 100 μg/mL streptomycin (Carl Roth, Karlsruhe, Germany). Prior to animal testing, low-passage stocks were titrated to Vero E6 cells using semi-solid overlay medium as described.[77] Briefly, Vero E6 cells were incubated with serial 10-fold dilutions of virus strains for 2 h. The virus inoculum was then replaced with an overlay medium consisting of Dulbecco's modified Eagle's medium (DMEM; PAN Biotech, Aidenbach, Germany), 2.5% microcrystalline cellulose (Avicel RC-591; DuPont, Wilmington, DE, USA) and 10% FBS. After 72 h of incubation at 37°C in a 5% CO_2 atmosphere, cells were fixed with 4% formaldehyde for 24 h and plaques were visualized by methylene blue counterstaining. Sequence integrity of virus stocks was determined by Illumina sequencing as described[78] and aligned to the isolate reference sequence (GenBank: MT270101 and GISAID: EPI_ISL_406862).

METHOD DETAILS

Animal experimentation

10- to 12-week-old male and female Syrian and Roborovski hamsters were infected intranasally with 1×10^5 or 1×10^4 plaque-forming units (pfu) SARS-CoV-2 (variant B1, isolate BetaCoV/Germany/BavPat1/2020) under anesthesia as previously described.[79] To prevent any prolonged suffering, the hamsters were clinically examined twice daily. Animals with body weight loss >15% for more than 48 h were euthanized according to the animal use protocol. Otherwise, naive hamsters (*n* = 3) and hamsters at 2, 3, 5, and 14 days post infection (*n* = 3 each) were randomly selected. Euthanasia was performed by cervical dislocation and exsanguination under anesthesia as previously described.[28] Among other materials, all lung lobes were collected for subsequent analyses. Specifically, the left lobe was used for histopathology, the right caudal lobe for single-cell analysis, the right cranial lobe for virological measurements, and the right middle lobe for bulk RNA and proteomic analysis as described.[19]

Single-cell isolation

Established cell isolation protocols were modified to comply with BSL-3 facility regulations. For single cell isolation, the caudal lobes of the right lung were stored in 1× PBS, 0.5% BSA containing 2 μg/mL actinomycin D. The lobes were dissociated mechanically and enzymatically. Tissue was first disrupted with forceps for 2 min in specific digestion medium (3.4 mg/mL collagenase Cls II (Merck), 1 mg/mL DNase I (PanReac AppliChem) in 2 mL Dispase medium per lung lobe (Corning), 50 caseinolytic units/mL) and then enzymatically digested at 37°C and 5% CO_2 for 30 min. The cell suspension was further dissociated by pipetting, and filtered through 70 μm cell strainers. The suspensions were centrifuged at 350 g for 6 min at 4°C, and the pellets were subjected to erythrocyte lysis by resuspension in appropriate buffer (BioLegend). The reaction was stopped by washing with PBS/BSA buffer and the cells were centrifuged. Cells were resuspended in low BSA buffer (1 × PBS, 0.04% BSA) and then filtered through 40 μm FloMi filters (Merck). Cell number and viability were determined microscopically using trypan blue.

Generation of single-cell RNA-sequencing data

Sequencing libraries were generated using the 3′ Chromium Next GEM Single Cell 3′ Reagent kit (10x Genomics) according to the manufacturer's instructions, and sequenced on a NovaSeq 6000 device (Illumina) to a depth of about 300 million reads per sample.

Histopathology

For histopathological evaluation, left lungs were immersion fixed in 10% buffered formalin (pH 7.0) for 48 h, processed overnight in a Tissue Tek robot, embedded in paraffin and cut at 2 μm thickness. Three sections per lung were obtained with a distance between adjacent planes of approximately 150 μm with the last section centrally placed at the tracheal bifurcation. Sections were stained with hematoxylin and eosin (H&E) as previously reported.[80] In addition, neutrophils were visualized using a naphthol AS-D chloroacetate

esterase (NACE) kit (Sigma-Aldrich, Germany) according to kit instructions. Bright field photomicrographs were taken with an Olympus BX41 microscope, a DP80 Microscope Digital Camera (Olympus, Hamburg, Germany), and cellSensTM Imaging Software, Version 1.18 (Olympus Soft Imaging Solutions). NACE signals were also assessed using an inverse microscope DMi8 CS Premium (Stellaris 8 FALCON, Leica, Germany) with an HC PL APO 63x/1.40 OIL CS2 (Art.-Nr.15506350, Leica, Germany) objective. Excitation at 590 nm was achieved with an STELLARIS 8 white light laser (WLL, pulsed, 440–790 nm). The wavelength detection range of a Power HyD S detector (Leica, Germany) was set from 600 to 750 nm. Trans multi-alkali photomultiplier tubes were turned on and the output color was set to gray. Smart gain was set to 26%. Microphotographs were taken with a Flash 4.0 V3 camera (Hamamatsu, Japan) and Las X Stellaris software (Leica, Germany) at original and additionally at three times digitally zoomed-in magnification. Pathologic changes were assessed by a board-certified, veterinary pathologist (ADG).

QUANTIFICATION AND STATISTICAL ANALYSIS

Data analysis was primarily performed using scanpy[70] (v1.9.1) and DESeq2[71] (v1.38.3). For integration we used scVI[72] (scvi-tools, v0.19.0). We relied on snakemake[76] (v7.20.0) to compose a reproducible and modular analysis pipeline using parallelized computations. Code used to analyze the data and produce figures is publicly available at https://github.com/stefanpeidli/PanCov19_Hamster. A version of record can be accessed from https://doi.org/10.5281/zenodo.11124622. Definitions of statistical significance or properties such as median and interquartile range are provided in the corresponding figure legends.

Processing of single-cell RNA-seq data
Raw scRNA-seq reads (FASTQ format) were aligned to reference genomes (Roborovski hamster[65] and Syrian hamster[66]) and quantified to produce a count matrix using CellRanger (v6.1.1) from 10X Genomics with default parameters. Filtered feature barcode matrices from cellranger count were read into scanpy. Raw counts were saved to 'adata.layers['counts']' for later use. We normalized counts using 'scanpy.pp.normalize_total' and log-scaled the results using 'scanpy.pp.log1p'. We did not Z score normalize the gene expression matrix. Doublets were identified and removed using scrublet (v0.2.3).[75] We used UMAP[81] for visual embeddings only, and diffusionmap[35,36] to generate latent spaces for further analysis. Gene signatures were called using scanpy.tl.score_genes.

Filtering, clustering, and cell type annotation
Following generation of count matrices using CellRanger, the data was further processed in R using Seurat.[73] For both hamster species, all samples were merged into one Seurat object, and cells grouped into 45–50 clusters. Based on known marker genes, clusters were annotated into broader cell type categories, or "mixed/unknown". Subsequently, clusters representing likely low quality cells, i.e., low UMI and gene counts, were discarded. In all other clusters, cells with less than the median of UMI counts, or more than the upper quartile plus three inter-quartile ranges (outliers) were discarded. In contrast to a general quality threshold based on UMI or gene counts, this introduces less bias as e.g., neutrophils have much lower UMI/gene counts than macrophages. After that first step, samples were integrated using the sctransform workflow,[82] and clustered again, to about 30 clusters. As before, these clusters were assigned to cell types using marker genes.

Differential expression analysis
We averaged unnormalized counts per sample and cell type in python and exported the resulting pseudo bulk count matrix to be used in the DESeq2 package[71] (v1.38.3) in R. We filtered out genes with less than 10 counts in total, and pseudo bulks obtained by summing over less than 10 cells to reduce the impact of outlier cells. Adhering to recommendations by DESeq2 authors on applications to scRNA-seq data, we used the following options: test = "LRT", minReplicatesForReplace = Inf. We compared all infected samples (2 and 3 dpi only for hamsters) against control/healthy samples separately for each hamster type and human dataset. Sample sizes for human and hamster samples of different severities and infection status can be found in Table S1 (see source files as listed in the key resources table), and lied between $2 < n < 15$ samples. DESeq2 results were then exported and analyzed in python, where we generally worked with results filtered by adjusted p-value of <0.05 if not otherwise noted.

Mapping orthologous genes between hamster and human genomes
Instead of "upper-casing" hamster genes to get human orthologs we used existing orthologies to map genes more accurately. We exported human and mouse orthologs from biomart,[67] since the hamster genomes used in this study were originally aligned against mouse genomes. For each hamster gene, we searched whether there were human orthologs in the database. If multiple were found, we used the best match according to orthology confidence reported by biomart. If no ortholog was found, we kept the gene name and upper-cased it as a best-guess matching.

Integration of hamster data with scVI
After concatenating all Syrian and Roborovski hamster scRNA-seq data, we identified the 2000 most highly variable genes using 'scanpy.pp.highly_variable_genes' on unnormalized counts using flavor = 'seurat_v3',[83] giving organism identity (Syrian/Roborovski) as batch_key. This selects for genes that are highly variable within Syrian and Roborovski and can be seen as a mild

form of batch effect correction. We ran scVI[72] with hamster type as batch_key without further covariate keys until convergence (early_stopping = True), with training/test/validation set size ratios of 90/5/5%, respectively. Integrations were both performed on all data and on subsets only (macrophages/endothelial cells/neutrophils) to achieve appropriate resolution in the scVI latent spaces in each case. When not otherwise mentioned, the scVI latent spaces were used for computing KNN graphs and therefore also for the KNN-based UMAP and diffusion map embeddings.

Diffusion analysis of neutrophils and endothelial cells

Diffusion map[35,36] is a non-linear dimensionality reduction method. Unlike other commonly used dimensionality reduction methods such as principal component analysis (PCA), diffusion map tries to find the longest paths (main axes of variation) in the data by wandering between cells on the K-nearest neighbor (KNN) graph. Distances between closely neighboring cells are used to model a random walk, where the probability to transition between cells is represented by a Gaussian kernel, i.e., it scales exponentially with the inverse of their distance. Cells that are not connected in the KNN graph will have a transition probability of zero between them. Mathematically, this random walk process on a microscopic level translates to a diffusion process on the macroscopic level,[84,85] hence the name diffusion map. While PCA performs eigendecomposition on the data's covariance matrix, diffusion map uses the same approach on the transition matrix defined by the diffusion process after some normalization steps. In both cases, this yields a list of eigenvectors, ranked by the value of the corresponding eigenvalues, defining the principle or diffusion components respectively. These components can then be interpreted, as is done for neutrophils and endothelial cells in this work using GSEA on genes (anti-) correlating with the components or distribution of specific cell groups along each component using histograms.

Post-hoc interpretation of diffusion components

We employed a simple strategy for post-hoc interpretation of latent variables using one-way ANOVA: Given a continuous or categorical explanatory variable per cell, for each latent variable we fit a simple linear regression model. We then computed how much variability between cells across the latent variable can be explained by the explanatory variable in this linear model as:

$$Variation\ Explained = 1 - \frac{RSS}{TSS} \times DOF_{adjustment}$$

with variables RSS: residual sum of squares, TSS: total sum of squares, and $DOF_{adjustment}$: degrees of freedom adjustment factor. These values were obtained from a simple uni-variate linear regression against each latent factor separately. As explanatory variables we used variables that we would expect to play a significant role in shaping the data by prior knowledge, e.g., cell cycle phases, virus detected, cell subtype, various signaling pathway scores,[25,27,68] or study variables such as days past infection, organism or virus dose. In essence, the resulting variation explained describes how much variation in the data can be explained by a linear model based on the current predictor such as cell subtype or cell cycle phase. We applied this post-hoc interpretation method to the latent variables produced by PCA of mean-shifted 2000 highly variable genes' (HVG) expression, scVI, and diffusion map on scVI. Among those, diffusion map resulted in high overall interpretability with latent variables explained by few distinct explanatory variables, whereas both PCA and scVI tended to have few latent dimensions explained by many overlapping explanatory variables.

Gene set enrichment analysis

For gene set enrichment analysis (GSEA)[23] we utilized the python package gseapy[74] (v0.10.8). For comparison between infected and control samples, results from DESeq2 (infected vs. control/healthy) were first filtered to exclude genes with less than 10 baseMean. The prerank module by gseapy takes in a ranked list of genes together with the score used for ranking them. As basis for the score we used negative log10 of *p*-values prior to multiple-testing correction, as this correction does not change the ranking except that it might lead to genes having ties in scores which should generally be avoided in GSEA. Subsequently, these values, representing the statistical strength of each gene's change, were multiplied by the sign of each gene's log fold change, representing the direction of change. This score was used to rank genes. For GSEA of neutrophils and endothelial cells, we ranked all genes by spearman correlation with the corresponding diffusion component. Afterward, we selected genes with a higher number of counts over all cells than the median to be considered. In both cases, ranked genes were given to gseapy.prerank, with parameters: min_size = 15, max_size = 1000, permutation_num = 1000. Gene sets used comprise KEGG_2021_Human[24] and MSigDB_Hallmark_2020.[27] GSEA results with an FDR q-value <0.05 were used for further analysis, including the normalized enrichment scores as direct output from gseapy.

Selection criteria and processing of human SARS-CoV2 scRNA-seq counts

We searched for scRNA-seq datasets of human patients with the following criteria: A control population must be provided, e.g., healthy patient samples; multiple disease severities must be present and annotated, e.g., mild and severe COVID-19; at least three samples per severity must be present; the data must represent a sample from the airways, which excludes blood samples. This resulted in three representative human datasets from BAL fluid, nasal swab, and postmortem tissue.

Count data for the datasets from Liao et al.[21] and Melms et al.[22] were retrieved from GEO, and the data from Chua et al.[20] was downloaded from figshare. A download bash script is provided in our code repository in GitHub, together with a jupyter notebook processing all three datasets. In summary, cells were filtered (1000 < UMI counts <30000; percent mitochondrial counts <30%), then library normalized and log1p transformed, followed by HVG selection, PCA, KNN calculation and UMAP embedding. Cell type annotations were provided by the original authors. The data from Melms et al. was already filtered. We note that the UMI counts per cell in that dataset were below 1000 counts for most cells, which is likely a consequence of the tissue obtained postmortem.